



<b>Publication Year</b>	2018
<b>Acceptance in OA</b>	2020-12-23T17:01:41Z
<b>Title</b>	Hunting for metals using XQ-100 Legacy Survey composite spectra
<b>Authors</b>	Perrotta, S., D'ODORICO, Valentina, Hamann, F., CRISTIANI, Stefano, Prochaska, J. X., Ellison, S. L., Lopez, S., CUPANI, Guido, Becker, G., Berg, T. A. M., Christensen, L., Denney, K. D., Worseck, G.
<b>Publisher's version (DOI)</b>	10.1093/mnras/sty2205
<b>Handle</b>	<a href="http://hdl.handle.net/20.500.12386/29185">http://hdl.handle.net/20.500.12386/29185</a>
<b>Journal</b>	MONTHLY NOTICES OF THE ROYAL ASTRONOMICAL SOCIETY
<b>Volume</b>	481

# Hunting for metals using XQ-100 Legacy Survey composite spectra

S. Perrotta,<sup>1,2★</sup> V. D’Odorico,<sup>2,3</sup> F. Hamann,<sup>1</sup> S. Cristiani,<sup>2,4</sup> J. X. Prochaska,<sup>5</sup> S. L. Ellison ,<sup>6</sup> S. Lopez,<sup>7</sup> G. Cupani,<sup>2</sup> G. Becker,<sup>1</sup> T. A. M. Berg,<sup>6</sup> L. Christensen ,<sup>8</sup> K. D. Denney<sup>9</sup> and G. Worseck<sup>10</sup>

<sup>1</sup>*Department of Physics and Astronomy, University of California, 900 University Avenue, Riverside, CA 92521, USA*

<sup>2</sup>*INAF–OATS, Via Tiepolo 11, 34143 Trieste, Italy*

<sup>3</sup>*Scuola Normale Superiore, Piazza dei Cavalieri 7, I-56126 Pisa, Italy*

<sup>4</sup>*INFN–National Institute for Nuclear Physics, via Valerio 2, I-34127 Trieste, Italy*

<sup>5</sup>*Astronomy & Astrophysics, UC Santa Cruz, 1156 High St., Santa Cruz, CA 95064, USA*

<sup>6</sup>*Department of Physics & Astronomy, University of Victoria, Finnerty Road, Victoria, British Columbia, V8P 1A1, Canada*

<sup>7</sup>*Departamento de Astronomia, Universidad de Chile, Casilla 36-D, Santiago, Chile*

<sup>8</sup>*Dark Cosmology Centre, Niels Bohr Institute, University of Copenhagen, Juliane Maries Vej 30, DK-2100 Copenhagen, Denmark*

<sup>9</sup>*Department of Astronomy, The Ohio State University, 140 West 18th Avenue, Columbus, OH 43210, USA*

<sup>10</sup>*Institut für Physik und Astronomie, Universität Potsdam, Karl-Liebknecht-Str. 24/25, D-14476 Potsdam, Germany*

Accepted 2018 August 10. Received 2018 August 9; in original form 2018 May 29

## ABSTRACT

We investigate the N v absorption signal along the line of sight of background quasars, in order to test the robustness of the use of this ion as the criterion to select intrinsic (i.e. physically related to the quasar host galaxy) narrow absorption lines (NALs). We build composite spectra from a sample of  $\sim 1000$  CIV absorbers, covering the redshift range  $2.55 < z < 4.73$ , identified in 100 individual sight lines from the XQ-100 Legacy Survey. We detect a statistically significant Nv absorption signal only within  $5000 \text{ km s}^{-1}$  of the systemic redshift,  $z_{\text{em}}$ . This absorption trough is  $\sim 15\sigma$  when only CIV systems with  $N(\text{CIV}) > 10^{14} \text{ cm}^{-2}$  are included in the composite spectrum. This result confirms that N v offers an excellent statistical tool to identify intrinsic systems. We exploit stacks of 11 different ions to show that the gas in proximity to a quasar exhibits a considerably different ionization state with respect to gas in the transverse direction and intervening gas at large velocity separations from the continuum source. Indeed, we find a dearth of cool gas, as traced by low-ionization species and in particular by Mg II, in the proximity of the quasar. We compare our findings with the predictions given by a range of CLOUDY ionization models and find that they can be naturally explained by ionization effects of the quasar.

**Key words:** galaxies: high-redshift – (galaxies:) intergalactic medium – (galaxies:) quasars: absorption lines.

## 1 INTRODUCTION

Quasar outflows have been increasingly invoked by popular evolution models to regulate both star formation in host galaxies and the accretion of material on to central supermassive black holes (SMBHs: e.g. Granato et al. 2004; Di Matteo, Springel & Hernquist 2005; Hopkins et al. 2016; Weinberger et al. 2017). A SMBH at the centre of a galaxy can produce a large amount of energy ( $\sim 10^{62}$  erg). Even if just a few per cent of the quasar bolometric luminosity were injected into the interstellar medium (ISM) of the host galaxy, it could have a significant impact on the host galaxy evolution

(Scannapieco & Oh 2004; Prochaska & Hennawi 2009; Hopkins & Elvis 2010). Such feedback offers a natural explanation for the observed mass correlation between SMBHs and their host galaxy spheroids (e.g. King 2003; McConnell & Ma 2013). However, the actual mechanisms of feedback remain highly uncertain.

Outflows are often studied in the rest-frame ultraviolet (UV) via blueshifted narrow absorption lines (NALs) defined by full width at half-maximum (FWHM)  $\lesssim 300 \text{ km s}^{-1}$ . These absorbers are ubiquitously found and detected in all active galactic nucleus (AGN) subclasses (e.g. Crenshaw et al. 1999; Ganguly et al. 2001; Vestergaard 2003; Misawa et al. 2007). The limitation of NALs is that they arise from a wide range of environments, from high-speed outflows to halo gas to physically unrelated gas or galaxies at large distances from the quasar. Those forming in the proximity of quasars pro-

\* E-mail: serenap@ucr.edu

vide valuable tools to study the gaseous environment of quasar host galaxies (e.g. D’Odorico et al. 2004; Wu et al. 2010; Berg et al. 2018).

With the aim of investigating quasar winds, we must select NALs that truly trace outflowing gas cautiously. The outflow/intrinsic origin of individual NALs can be inferred from the following: (i) time variability of line profiles, (ii) absorption profiles significantly broader and smoother compared with the thermal line widths, (iii) high space densities measured directly from excited-state fine-structure lines, (iv) partial coverage of the background emission source measured via resolved, optically thick lines with too-shallow absorption troughs and (v) higher ionization states than intervening absorbers. Nonetheless, NALs can still be connected to the quasar host galaxy without exhibiting such properties (Hamann et al. 1997).

Previous works have shown that, among the highly ionized absorption species commonly used to identify outflows (e.g. C IV  $\lambda\lambda$ 1548, 1550; Si IV  $\lambda\lambda$ 1393, 1402; N V  $\lambda\lambda$ 1238, 1242; O VI  $\lambda\lambda$ 1031, 1037), N V is detected with the lowest frequency, but with the highest intrinsic fraction. Misawa et al. (2007) derived an intrinsic fraction of 75 per cent for N V NALs, through partial coverage and line-locking methods. Ganguly et al. (2013), using the same techniques, found a value of 29–56 per cent and suggested using this ion in building large catalogues of intrinsic NALs with lower resolution and/or lower signal-to-noise ratio (S/N) data.

In Perrotta et al. (2016, hereafter P16) we used the spectra of 100 quasars at emission redshift  $z_{\text{em}} = 3.5\text{--}4.72$  to build a large, relatively unbiased, sample of NALs and study their physical properties statistically. The spectra have been obtained with the echelle spectrograph X-shooter (Vernet et al. 2011) on the European Southern Observatory (ESO) Very Large Telescope (VLT) in the context of the XQ-100 Legacy Survey (López et al. 2016). P16 showed that N V is a key line to study the effects of the quasar ionization field, offering an excellent statistical tool for identifying outflow/intrinsic candidate NALs. Indeed, most of the N V systems in our sample exhibit distinctive signatures of their intrinsic nature with respect to intervening NALs (described above), and N V/C IV column density ratios larger than 1 (see Fechner & Richter 2009).

The large number of Ly $\alpha$  lines characterizing the forest in the spectra of quasars at  $z_{\text{em}} = 3.5\text{--}4.72$  prevents us in P16 from searching for individual N V lines at large velocity offsets (we could reliably identify N V only within  $5000 \text{ km s}^{-1}$  of  $z_{\text{em}}$ ). Most of the Ly $\alpha$  forest is associated with moderate overdensities and traces filamentary structure on large scales, but some strong forest absorbers, along with Lyman-limit systems (LLSs,  $N(\text{H I}) \geq 10^{17.2} \text{ cm}^{-2}$ ) and damped Lyman alpha absorptions (DLAs:  $N(\text{H I}) \geq 10^{20.3} \text{ cm}^{-2}$ ), are thought to be associated with galaxies and the circumgalactic medium (CGM: e.g. Faucher-Giguère & Kereš 2011; Fumagalli et al. 2011). Therefore, intervening metals associated with Ly $\alpha$  absorbers can probe different environments: from the ISM to the outer regions of galaxies (the CGM) far from the quasar to the more diffuse intergalactic medium (IGM).

In this work, we apply the stacking technique to the XQ-100 spectra to look for N V at large velocity separations from  $z_{\text{em}}$ . Indeed, when an ensemble of independent sight lines is stacked to produce a composite spectrum, the numerous stochastic H I absorptions average together and the resulting spectrum is flat, revealing any strong metal signal buried within the Ly $\alpha$  forest. These measurements will complement our previous study on N V and test the robustness of our claim on the use of N V as a criterion to select intrinsic NALs.

The work is organized as follows: Section 2 describes our methodology for identifying NALs; Section 3 collects the details of the

procedure followed to build the stacking spectra. Our results are presented in Section 4 and Section 5 discusses the original findings of our study. Our conclusions are summarized in Section 6.

We adopt a  $\Lambda$ CDM cosmology throughout this manuscript, with  $\Omega_{\text{M}} = 0.315$ ,  $\Omega_{\Lambda} = 0.685$  and  $H_0 = 67.3 \text{ km s}^{-1} \text{ Mpc}^{-1}$  (Planck Collaboration et al. 2014).

## 2 DATA

To carry out the study of N V absorption systems, we start from the C IV sample that we collected in P16. The C IV NALs are identified in quasar spectra from the XQ-100 Legacy Survey (López et al. 2016). The most common metal transition found in quasar spectra is C IV. Roughly half of the Ly $\alpha$  forest with  $N(\text{H I}) \geq 10^{14.5} \text{ cm}^{-2}$  is C IV-enriched at  $z \sim 3$  (Cowie et al. 1995; Songaila 1998). C IV enrichment has even been suggested at lower  $N(\text{H I})$  (Songaila 1998; Ellison et al. 2000; Schaye et al. 2003; D’Odorico et al. 2016). This is the main reason why we start our analysis from a sample of C IV absorbers, as well as better alignment of C IV systems with other metal lines with respect to Ly $\alpha$  absorbers (Kim et al. 2016).

In P16, we identify almost one thousand C IV doublets (1548.204, 1550.78  $\text{\AA}^1$ ) covering the redshift range  $2.55 < z < 4.73$ . The catalogue is produced with the goal of mapping the incidence of NALs in the quasar rest-frame velocity space. Our study includes any C IV absorber outside the Ly $\alpha$  forest in each spectrum (up to  $\sim 71\,580 \text{ km s}^{-1}$  from  $z_{\text{em}}$ ). We refer to systems occurring at less than  $5000 \text{ km s}^{-1}$  from the systemic redshift of the quasar as *associated* absorption lines (AALs).

We refer to P16 for a complete description of the identification and measurement of equivalent width (EW) and column density ( $N$ ) of C IV absorbers.

The absorber velocity ( $v_{\text{abs}}$ ) with respect to quasar systemic redshift is computed by the relativistic Doppler formula,

$$\beta \equiv \frac{v_{\text{abs}}}{c} = \frac{(1 + z_{\text{em}})^2 - (1 + z_{\text{abs}})^2}{(1 + z_{\text{em}})^2 + (1 + z_{\text{abs}})^2}, \quad (1)$$

where  $z_{\text{em}}$  and  $z_{\text{abs}}$  are the emission redshift of the quasar and the absorption redshift of the NAL, respectively, and  $c$  is the speed of light.

Our final sample includes 986 C IV doublets with  $-1000 < v_{\text{abs}} < 71\,580 \text{ km s}^{-1}$  and equivalent widths  $0.015 \text{ \AA} < \text{EW} < 2.00 \text{ \AA}$ .

Thanks to the high S/N and wavelength extent of our spectra, we are able to search for other common ions (N V, Si IV, C II, etc.) at the same redshifts as the detected C IV absorbers. However, contamination by the Ly $\alpha$  forest prevents us from investigating the same velocity range for all ions. In particular, our final sample consists of 46 N V absorbers with column density down to  $\log N(\text{N V}) \sim 12.8 \text{ cm}^{-2}$ , corresponding to a probability of 38 per cent of finding a N V at the same  $z_{\text{abs}}$  as a given C IV NAL with  $v_{\text{abs}} < 5000 \text{ km s}^{-1}$ . 55 per cent of N V systems have column densities larger than  $\log N(\text{N V}) > 14 \text{ cm}^{-2}$  and 85 per cent have values larger than  $\log N(\text{N V}) > 13.5 \text{ cm}^{-2}$ . Furthermore, 68 per cent of N V NALs have column densities larger than the corresponding C IV.

## 3 STACKING PROCEDURE

We adopt the stacking technique to explore the presence of a N V signal in the Ly $\alpha$  forest associated with the C IV absorbers de-

<sup>1</sup>Wavelengths and oscillator strengths used in this work are taken from Morton (2003).

scribed in the previous section. The first step to produce the stacked spectrum is the continuum normalization of all XQ-100 quasar spectra. The continuum placement in the Ly $\alpha$  forest is highly subjective, due to few portions of the spectrum being free from absorption (e.g. Kirkman et al. 2005). The continuum is particularly difficult to identify at the position of DLAs. The estimate of the continuum level is done manually by selecting points along the quasar continuum free of absorption (by eye) as knots for a cubic spline. For all sightlines, the continuum placement is inspected visually and adjusted such that the final fit resides within the variations of regions with clean continuum. Then, the flux and error arrays are continuum-normalized. The accuracy of the fits is as good as or better than the S/N of these clean continuum regions (see López et al. 2016 for a detailed description of the procedure adopted).

We follow the subsequent scheme for the construction of the average spectrum.

(i) For each of the 986 C IV systems identified in P16, we consider the position of the velocity component with the highest optical depth of the absorption profile as the redshift of the system,  $z_{\text{abs}}$ , around which we select the spectrum region to stack. For completeness, we will show how the results change when calculating the barycentre position of the system weighting the wavelengths with the optical depth of the line profile (see Section 4.4).

(ii) We use the C IV centre,  $z_{\text{abs}}$ , to select the region of the spectrum where the corresponding N V doublet should be located. Specifically, we select a region of  $\pm 1000 \text{ km s}^{-1}$  around the expected position of the N V centre (for both doublet components, i.e. N V  $\lambda 1238$  and N V  $\lambda 1242$ ).

(iii) Each selected region is shifted to the corresponding  $z_{\text{abs}}$  rest frame.

(iv) We generate a rest-frame wavelength array with fixed wavelength step  $\Delta\lambda$ . The step value is set to be slightly larger than the pixel size of the UV spectra. The visible arm of X-shooter has a mean resolution of  $\lambda/\Delta\lambda = 8800$ , while in the UV it goes down to  $\sim 5000$ . Thus, a region with the same extent is sampled with a larger number of pixels in the visible than in the UV region of the spectrum.

(v) For each selected spectral region, we compute the contribution of each pixel to the cells of the final grid.

(vi) All the flux values in each cell of the final grid are then averaged to produce the stacked spectrum.

(vii) Uncertainties in the observed stack are estimated through the bootstrap resampling technique. From a given number,  $N$ , of rest-frame spectral regions, we consider the first pixel of each region as the element of an array. We randomly sample from this array, allowing for replacement, to form a new sample (called a bootstrap sample) that is also of size  $N$ . This process is repeated a large number of times (e.g. 1000 times) and for each of these bootstrap samples we compute its mean. We now have a histogram of bootstrap means. This provides an estimate of the shape of the distribution of the mean. The measured standard deviation of this distribution is the error we associate with the first pixel of the stacked spectrum. Then, the method is applied to all the pixels of the rest-frame spectral regions to be stacked.

Our study is not so sensitive to continuum placement, because we perform the analysis relative to the average IGM opacity, without the goal of measuring the opacity.

For each sightline, we mask out the regions that have clear strong absorption features (i.e. Lyman breaks, sub-DLAs with  $N(\text{HI}) \sim 10^{19-20.3} \text{ cm}^{-2}$  and DLAs) when they coincide with those to be stacked. In particular, we take advantage of the DLA identification

performed by Sánchez-Ramírez et al. (2016). We define the extremes of the DLA absorption at the wavelengths where the wings of the DLA again match the level of the continuum to within the values of the flux error array.

We exclude 77 N V regions because they completely or partially overlap with Lyman breaks or DLA and sub-DLA absorptions. Our final sample consists of 909 N V selected regions, the centre of which is within  $-1000 < v_{\text{abs}} < 71\,580 \text{ km s}^{-1}$  of  $z_{\text{em}}$ . We extend the explored velocity range to  $-1000 \text{ km s}^{-1}$  to take uncertainties in the quasar systemic redshift into account (López et al. 2016) and to consider possible inflows.

This method is powerful in detecting even weak absorption features in the Ly $\alpha$  forest, where confusion noise from forest absorption lines makes it very difficult to identify individual metal lines reliably. However, N V is one of the most rarely detected ions in optically thin (i.e.  $N(\text{HI}) \lesssim 10^{17} \text{ cm}^{-2}$ ) intergalactic absorption systems and its signal is diluted if we stack regions selected within any velocity shift from  $z_{\text{em}}$  up to  $71\,580 \text{ km s}^{-1}$ .

## 4 RESULTS

The following sections collect the results of the search for metal absorptions corresponding to C IV clouds with  $10^{11.5} < N(\text{CIV}) < 10^{16.5} \text{ cm}^{-2}$  (see P16). We first investigate the presence of a N V signal as a function of the velocity shift from the quasar to test the nature of N V. Then, we examine many other lower and higher ionization species. The main goal is to characterize the ionization state of the gas both close and far from the continuum source.

### 4.1 N v absorption

The left panel of Fig. 1 shows the results for C IV and N V absorbers obtained by stacking the whole sample of sight lines. The zero velocity point,  $v = 0 \text{ km s}^{-1}$ , represents the  $z_{\text{abs}}$  of the deepest component of the corresponding C IV system. The average spectrum appears quite flat for both components of the N V doublet, as expected in the absence of a strong signal, due to the stochastic nature of the Ly $\alpha$  forest. The continuum level is decreased to a value below 1 due to the cumulative effect of Ly $\alpha$  forest absorption.

The right panel of Fig. 1 exhibits the C IV and N V composite spectra derived from the stacking of the regions corresponding to C IV NALs with  $N(\text{CIV}) \geq 10^{14} \text{ cm}^{-2}$ . This column density threshold matches the value we use in P16 to distinguish between weak and strong C IV systems. Selecting the strongest systems in the sample, we see only a small hint of coherent absorption features in the profile of the two N V doublet components. Fig. 1 combines all of the NALs regardless of velocity shift. In the following, we investigate the presence of a N V signal as a function of the velocity separation from the quasar to understand when it becomes significant. To this end, we produce N V composite spectra in bins of velocity offset from  $z_{\text{em}}$ .

Fig. 2 shows the stacked spectra of C IV and N V absorbers with  $-1000 < v_{\text{abs}} < 5000 \text{ km s}^{-1}$  and as a function of the corresponding  $N(\text{CIV})$ . In particular, in the left panels the stacked regions are selected so that  $N(\text{CIV}) < 10^{14} \text{ cm}^{-2}$ , while in the right ones  $N(\text{CIV}) \geq 10^{14} \text{ cm}^{-2}$ . The first column density threshold chosen for the stacking produces a hint of coherent absorption in the profile of both N V components (left panels). The signal of the absorption line is weak, but represents a  $4\sigma$  detection. The N V composite spectrum shows the N V lines clearly present at  $> 15\sigma$  confidence once only the regions corresponding to the strongest C IV are selected to be stacked (right panels). We note that both N V lines display the same

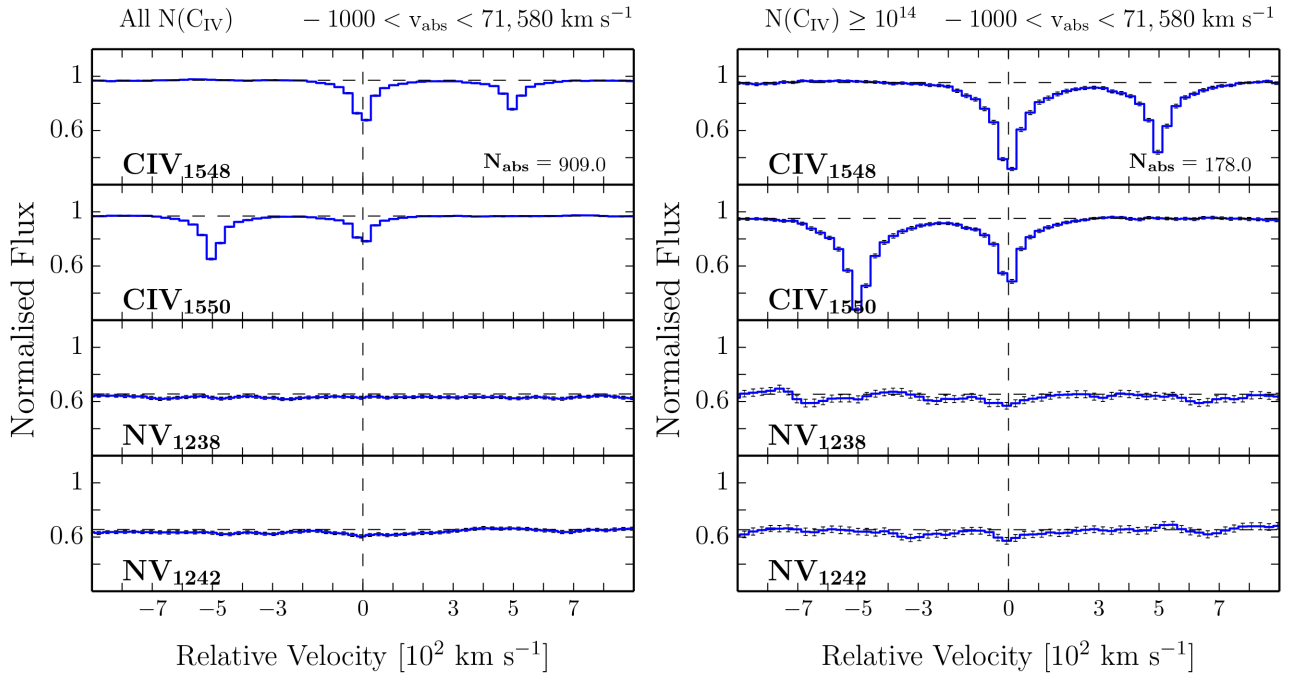


**Figure 1.** Left: average absorption-line spectra for CIV and NV, selected within any velocity separation from  $z_{\text{em}}$ .  $N_{\text{abs}}$  indicates the number of absorbers considered to build the stacked spectrum. Right: same as for the left panels, but in this case only regions corresponding to the strongest CIV NALs (i.e.  $N(\text{CIV}) \geq 10^{14} \text{ cm}^{-2}$ ) are included in the stack. Error bars are  $1\sigma$  and are estimated by bootstrapping the data using 1000 realizations.

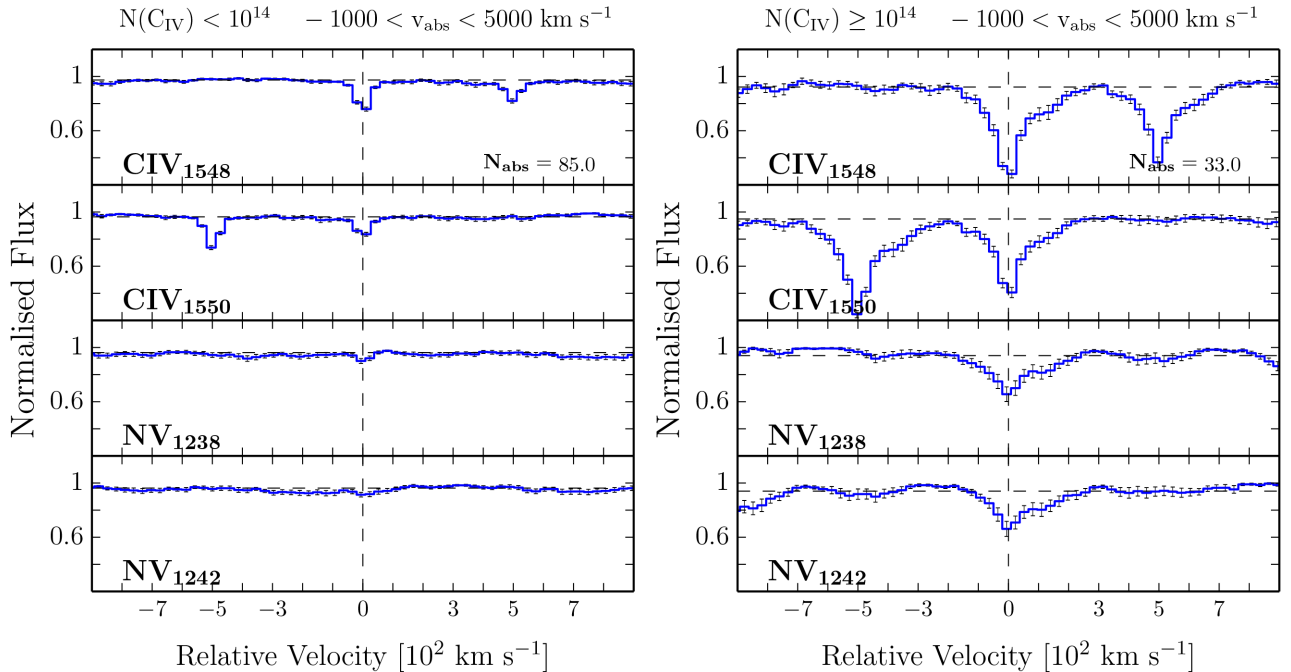


**Figure 2.** Left: average absorption-line spectra for CIV and NV selected within  $5000 \text{ km s}^{-1}$  of  $z_{\text{em}}$ . Only regions corresponding to CIV NALs with  $N(\text{CIV}) < 10^{14} \text{ cm}^{-2}$  are included in the stack.  $N_{\text{abs}}$  indicates the number of absorbers considered to build the stacked spectrum. Right: same as for the left panels, but in this case  $N(\text{CIV}) \geq 10^{14} \text{ cm}^{-2}$  is considered as the threshold for the stacking. Error bars are  $1\sigma$  and are estimated by bootstrapping the data using 1000 realizations.

kinematic profile and they also match those of the corresponding CIV NAL.

The associated region is the only spectral window in which we are able to identify individual NV NALs. The number of CIV doublets within  $5000 \text{ km s}^{-1}$  of  $z_{\text{em}}$  as a function of the column density is re-

ported in Table 1, as well as the fraction of CIV showing associated NV. The stronger the CIV column density, the higher the probability of selecting systems with NV at the same redshift. This trend is not due to a detection bias affecting the identification of NV NALs at low column densities. Indeed, the high and uniform S/N of the

**Table 1.** Probability that an individual C IV NAL within  $5000 \text{ km s}^{-1}$  of  $z_{\text{em}}$  shows a NV absorber at the same absorption redshift, as a function of its column density.

	Number of C IV <sup>a</sup>	C IV with NV <sup>b</sup>
All	122	38%
$\log N(\text{C IV}) \geq 14.3$	25	72%
$\log N(\text{C IV}) \geq 14$	42	55%
$\log N(\text{C IV}) \geq 13.5$	85	44%
$\log N(\text{C IV}) < 14.3$	97	29%
$\log N(\text{C IV}) < 14$	80	29%

<sup>a</sup>Number of C IV NALs with  $v_{\text{abs}} < 5000 \text{ km s}^{-1}$  and with column density in the selected range.

<sup>b</sup>Fraction of C IV NALs with a NV absorber at the same absorption redshift. The detection limit on NV is  $\log N(\text{NV}) \sim 12.8 \text{ cm}^{-2}$ .

XQ-100 spectra allows us to identify NV systems reliably down to  $\log N(\text{NV}) \sim 12.8 \text{ cm}^{-2}$  (see P16). In addition, associated NV NALs are preferentially stronger than the corresponding C IV (Fechner & Richter 2009). However, we adopt  $N(\text{C IV}) = 10^{14} \text{ cm}^{-2}$  as the column density threshold to distinguish between weak and strong systems. This restriction is motivated by the requirement to have a minimum number of systems within a given velocity separation from  $z_{\text{em}}$  to build the composite spectrum. This is crucial, especially when we investigate large velocity offsets from  $z_{\text{em}}$ , where the number density of C IV NALs exhibits a clear drop with respect

to the excess of lines found in proximity to the quasar (see P16). Moreover, Fechner & Richter (2009) have shown that intervening NV systems are systematically weaker than the associated ones: no intervening NV system with  $N(\text{NV}) \geq 10^{14} \text{ cm}^{-2}$  has been detected. It is therefore very important to explore the regime of weak lines.

To investigate the NV signal beyond the associated region, we build the NV composite spectra in bins of  $5000 \text{ km s}^{-1}$  up to  $71580 \text{ km s}^{-1}$  from  $z_{\text{em}}$  for both weak and strong C IV systems. In particular, Fig. 3 (left column) shows the results for C IV and NV absorbers with  $10000 < v_{\text{abs}} < 15000 \text{ km s}^{-1}$ . The stacked spectra produced selecting only C IV systems with  $N(\text{C IV}) \leq 10^{14} \text{ cm}^{-2}$  are presented in the top panel, while in the bottom one only C IV systems with  $N(\text{C IV}) \geq 10^{14} \text{ cm}^{-2}$  are considered. In both cases, there is no imprint of any significant coherent absorption feature in the profile of the two NV doublet components. We show just one of the many  $5000 \text{ km s}^{-1}$  velocity bins studied, because they all exhibit the same behaviour. Fig. A5 in the Appendix demonstrates that the stacking technique applied to the XQ-100 spectra is actually able to detect absorption lines in the Ly $\alpha$  forest.

We then consider larger velocity bins, in order to increase any possible signal of intervening NV absorbers. This is particularly important for strong systems, which are much rarer at large separations from the quasar (see P16). The stacked spectra produced selecting only C IV systems with  $15000 < v_{\text{abs}} < 25000 \text{ km s}^{-1}$  ( $10000 < v_{\text{abs}} < 35000 \text{ km s}^{-1}$ ) are presented in the middle column of Fig. 3 (right column of Fig. 3).

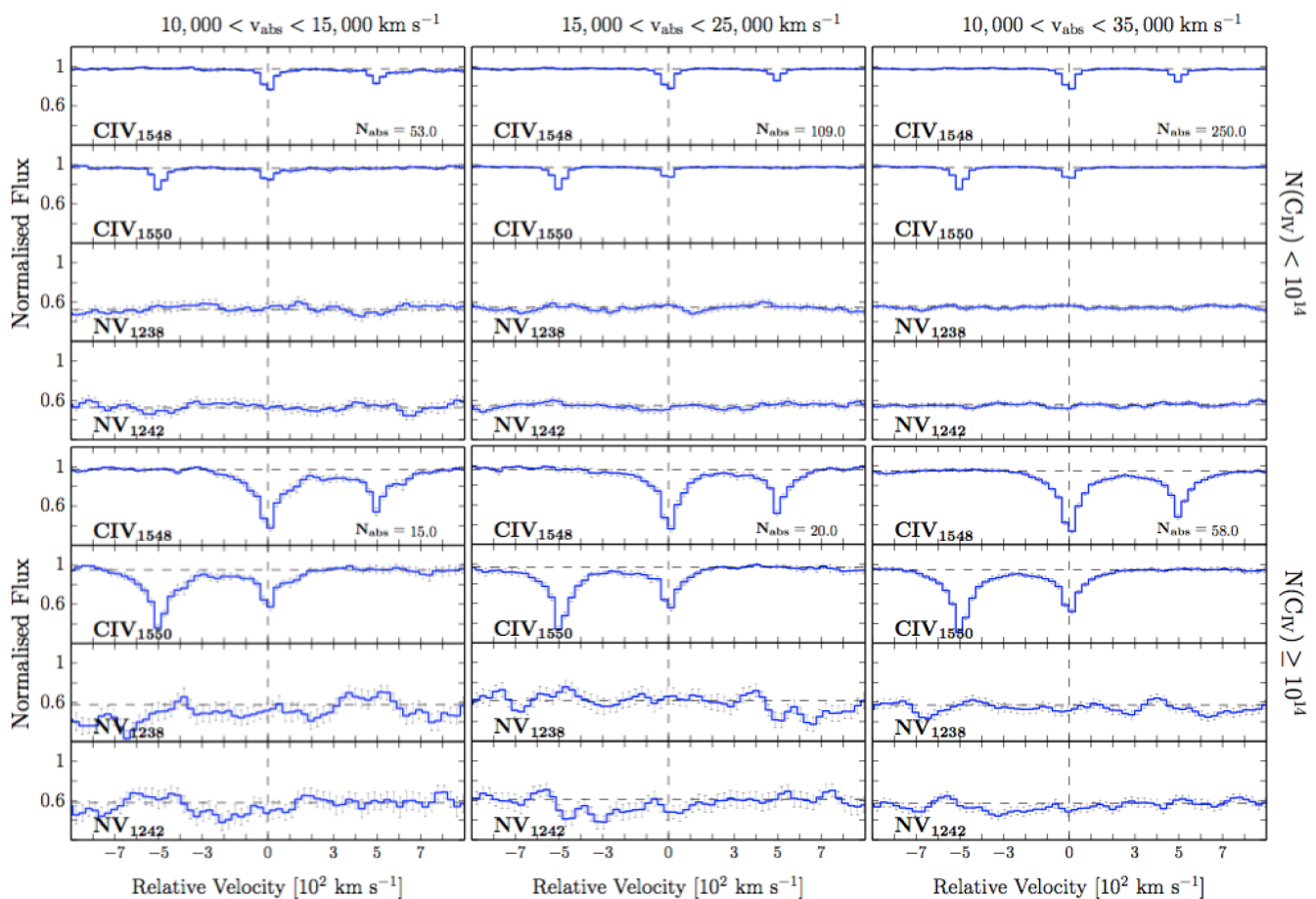


**Figure 3.** Top panels: the average absorption-line spectra produced selecting only C IV systems with  $N(\text{C IV}) \leq 10^{14} \text{ cm}^{-2}$  are shown in different bin sizes of velocity offset from  $z_{\text{em}}$ . Bottom panels: same as for the top panels, but with a different column density threshold,  $N(\text{C IV}) \geq 10^{14} \text{ cm}^{-2}$ .

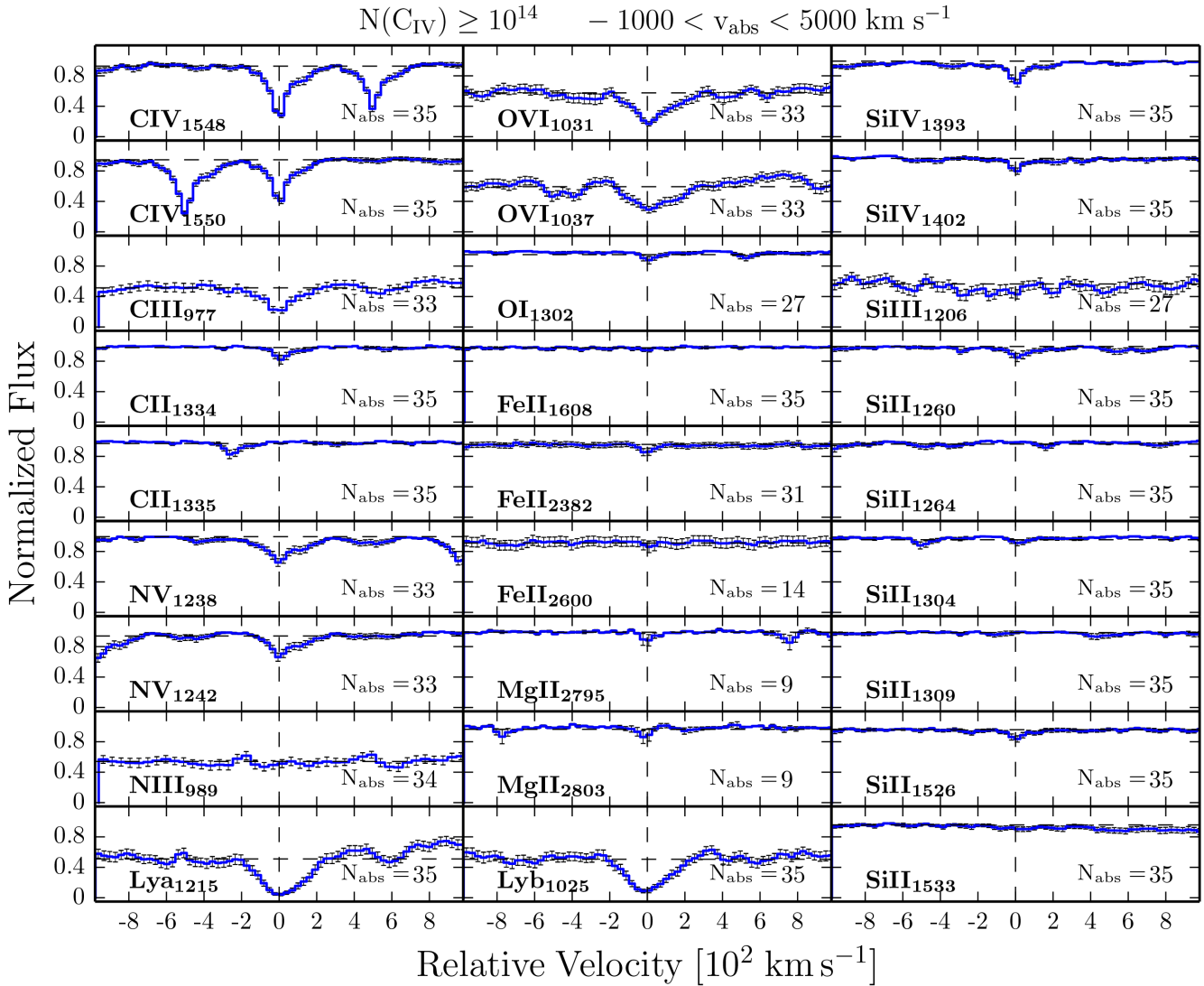


**Figure 4.** Composite spectra for the ions studied in this work, based on C IV systems with  $N(\text{CIV}) \geq 10^{14} \text{ cm}^{-2}$  and  $-1000 < v_{\text{abs}} < 5000 \text{ km s}^{-1}$ . Every panel reports the number of absorbers considered to build the stacked spectrum.  $N_{\text{abs}}$  is not the same for all ion species, because each one undergoes a different masking for DLA, sub-DLA and Lyman breaks. The error bars are  $1\sigma$  and are estimated by bootstrapping the data using 1000 realizations. We include Mg II and Fe II  $\lambda 2600$  lines despite them both suffering from poor statistics.

The absence of statistically significant intervening N V absorption is a common feature independent of the parameters ( $N(\text{CIV})$  and  $v_{\text{abs}}$ ) selected as threshold of the stacking. The mean rest-frame EW upper limit found for the N V absorption line in different velocity bins explored is  $\sim 0.03 \text{ \AA}$ . This finding strongly suggests that a proximity of  $5000 \text{ km s}^{-1}$  from the quasar is required for N V to be detected.

#### 4.2 Other metal species

Besides the stacked spectra to detect N V absorptions, we have computed with the same technique the stacked spectra for the following transitions associated with the sample of detected C IV lines: Ly $\alpha$   $\lambda 1215.67 \text{ \AA}$ , Ly $\beta$   $\lambda 1025.72 \text{ \AA}$ , C III  $\lambda 977.02 \text{ \AA}$ , C II  $\lambda 1334.53 \text{ \AA}$ , O I  $\lambda 1302.16 \text{ \AA}$ , Si III  $\lambda 1206.50 \text{ \AA}$ , Si II  $\lambda 1260.42, 1304.37, 1526.70 \text{ \AA}$ , Fe II  $\lambda 2382.76 \text{ \AA}$  absorption and Si IV  $\lambda\lambda 1393.76, 1402.77 \text{ \AA}$ , O VI  $\lambda\lambda 1031.92, 1037.61 \text{ \AA}$  and Mg II  $\lambda\lambda 2796.35, 2803 \text{ \AA}$  doublet absorption.

The composite spectrum based on C IV systems with  $N(\text{CIV}) \geq 10^{14} \text{ cm}^{-2}$  and  $-1000 < v_{\text{abs}} < 5000 \text{ km s}^{-1}$  is shown in Fig. 4. Based on ionization arguments, we would expect that C IV NALs showing associated ions like N V or O VI ought not to have low-ionization transitions. To remove the effects of DLAs on our investigation, we exclude all C IV associated with DLAs (Sánchez-Ramírez et al. 2016) from the stacking. As a consequence, we do not see any significant evidence of absorption trough in the spectra of C II, Mg II, Si II, Fe II and O I (see Fig. A3). This result is expected, since we have already measured a C II covering fraction of 10 per cent for absorbers with  $v_{\text{abs}} < 10000 \text{ km s}^{-1}$  along the line of sight (P16), in contrast with what is observed in the transverse direction (Prochaska, Lau & Hennawi 2014). This finding seems to be confirmed by the absence of a strong Mg II signal in the proximity of the quasar. We will come back to this point in Section 4.3.

To quantify the detections clearly present in the composite spectrum, we measure the equivalent widths of the absorption lines. The continuum is first established by fitting a cubic spline function

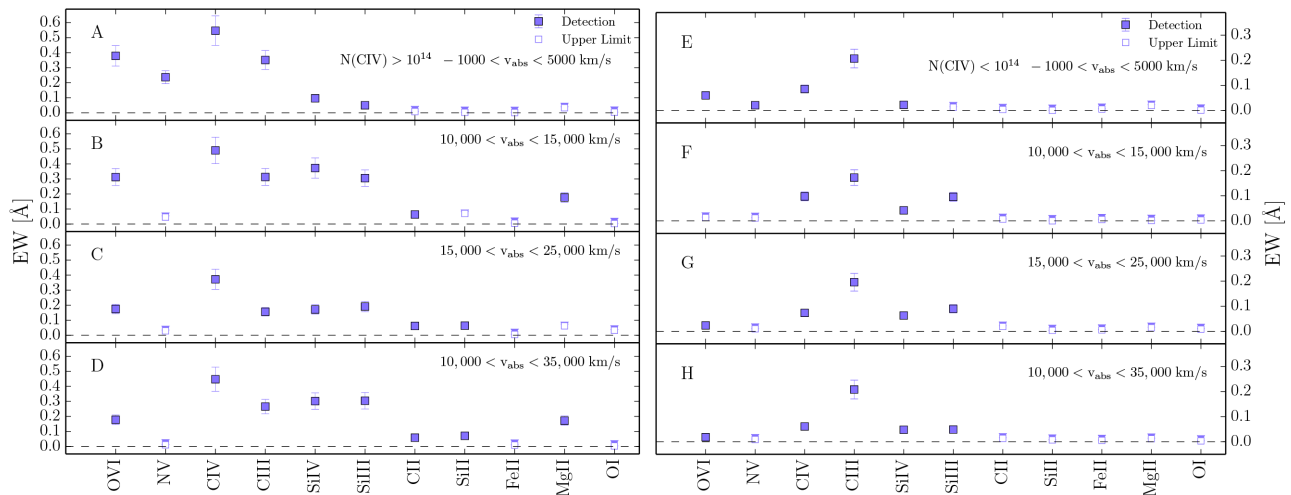


**Figure 5.** Left: equivalent widths of metal species measured in order of decreasing ionization potential for composite spectra based on C IV systems with  $N(\text{C IV}) \geq 10^{14} \text{ cm}^{-2}$ . Each panel displays an increasing velocity offset from  $z_{\text{em}}$  and bin size, going from top to bottom. C IV DLAs have been excluded from the stacking. Right: same as for the left panels, but in this case C IV systems with  $N(\text{C IV}) < 10^{14} \text{ cm}^{-2}$  are included in the stack. The EW refers only to the strongest member of the doublets. Error bars are  $1\sigma$  and are estimated by bootstrapping the data using 1000 realizations.

to the spectral regions free of apparent absorption lines. Then, the rest-frame equivalent width is measured as described in Section 2. We present our metal-line equivalent width measurements in Fig. 5. For those lines that are not detected at over  $3\sigma$  significance level, we give the  $3\sigma$  upper limits on their equivalent widths.

The left panels of Fig. 5 show the equivalent widths derived for composite spectra based on C IV systems with  $N(\text{C IV}) \geq 10^{14} \text{ cm}^{-2}$ . Each panel displays an increasing velocity offset from  $z_{\text{em}}$  going from top to bottom. In panels (c) and (d), we examine larger velocity bins, to allow low-ionization ions to be sufficiently numerous to produce measurable absorptions. In the proximity of the quasar (Fig. 5a), we detect species with ionization potentials down to and including Si IV and intermediate lines such as Si III. Moving further from the associated window (Fig. 5b–d), we no longer see NV; this result is insensitive to the bin size chosen, as already shown in Section 4.1. However, we do detect O VI independently of the velocity bin size and the velocity shift from  $z_{\text{em}}$ .

Looking at increasing velocity offsets from  $z_{\text{em}}$ , we can see how the quasar radiation field affects the gas along the propagation axis of the outflows. Indeed, low-ionization species (like C II, Si II, Mg II) are mainly present in our strongest C IV absorption sample when we move further from the associated region (Fig. 5b–d). In Fig. 5(a) we examine gas more directly influenced by the quasar radiation. Closer to the emission of the quasar, the radiation field is more intense and the gas is more highly ionized (assuming a similar gas density); it is thus reasonable to expect that the occurrence of low-ionization lines decreases there.

The number of strong C IV systems steeply decreases beyond  $5000 \text{ km s}^{-1}$  from  $z_{\text{em}}$  (Perrotta et al. 2016). Thus, if we consider an individual velocity bin size of  $5000 \text{ km s}^{-1}$  along the line of sight, it can happen that some isolated line dominates the signal of a given ion (e.g. see the Si IV, Si III and Mg II lines in Fig. 5b). In particular, Mg II and Fe II  $\lambda 2600$  are the ions that suffer the most poor statistics, due to their location in the near-IR. Indeed, their expected positions often coincide with deep atmospheric absorption bands that do not allow us to include those systems in the stacking. This is the main reason for exploring larger velocity bins. Increasing the statistics of systems that build the composite spectrum, we are more confident to catch the general behaviour of the ions. When we consider larger bin

size (Fig. 5c and d), we do detect low-ionization potential species such as C II, Si II and Mg II, in agreement with previous works based on composite spectra (e.g. Lu & Savage 1993; Prochaska, O’Meara & Worseck 2010; Pieri et al. 2010, 2014).

The right panels of Fig. 5 show the equivalent widths derived for composite spectra based on C IV systems with  $N(\text{C IV}) < 10^{14} \text{ cm}^{-2}$ . Each panel displays an increasing velocity offset from  $z_{\text{em}}$  and bin size, going from top to bottom. DLAs of C IV have been excluded from the stack. The C IV sample exploited in this work shows a statistically significant excess within  $10000 \text{ km s}^{-1}$  of  $z_{\text{em}}$  with respect to the random incidence of NALs, which is especially visible for weak lines (Perrotta et al. 2016). The observed excess includes contributions from the following: (i) outflowing gas that is ejected from the central AGN, (ii) intervening absorbers physically related to the galaxy haloes that cluster with the quasar host and (iii) environmental absorption, which arises in either the ISM of the quasar host galaxy or the IGM of the galaxy’s group or cluster. Most likely, C IV systems showing a NV absorber at the same redshift are intrinsic. We do not detect low-ionization ions within the associated window, nor moving further from  $z_{\text{em}}$  (Fig. 5f–h). This is true independently of the velocity bin size chosen. Low-ionization metal transitions, such as Mg II and C II, are mostly found at  $N(\text{H I}) \geq 10^{16} \text{ cm}^{-2}$  (e.g. Farina et al. 2014). Therefore, most of the weak C IV systems in our sample are probably associated with  $N(\text{H I}) < 10^{16} \text{ cm}^{-2}$  (see also Kim et al. 2016; D’Odorico et al. 2016). In addition, we detect O VI only if we consider a velocity bin width of at least  $10000 \text{ km s}^{-1}$ , although its signal is weak.

### 4.3 Mg II covering fraction

Various studies based on projected quasar pairs agree that quasar host galaxies at  $z > 1$  exhibit a high incidence of optically thick, metal-enriched absorption systems traced by H I Ly $\alpha$ , C II, C IV and Mg II absorption along the transverse direction at  $d \lesssim 300 \text{ kpc}$ , but low incidence along the foreground quasar sightline itself (Bowen et al. 2006; Hennawi et al. 2006; Shen & Ménard 2012; Farina et al. 2013, 2014; Hennawi & Prochaska 2013; Prochaska et al. 2014; Lau, Prochaska & Hennawi 2016; Lau, Prochaska & Hennawi 2018; Chen et al. 2018). This contrast indicates that the ionizing emission

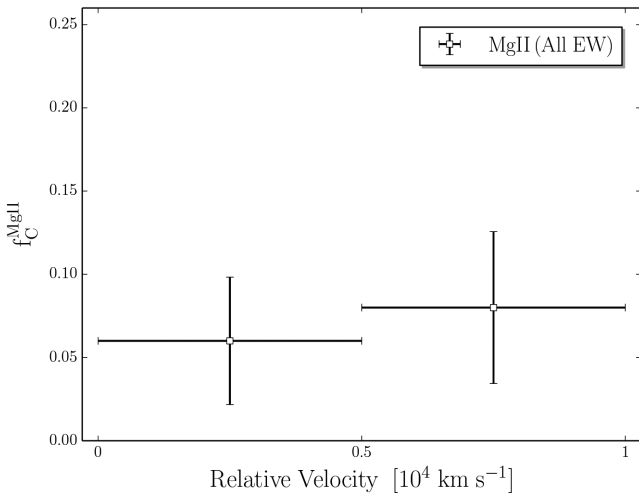


**Figure 6.** Covering fraction,  $f_C$ , for Mg II  $\lambda 2796$  estimated from the fraction of quasars exhibiting at least one absorber in bins of velocity offset from  $z_{em}$ . The rest-frame equivalent width detection limit (in the near-IR) in our sample is  $0.036 \text{ \AA}$  (see P16).

from quasars is highly anisotropic, in qualitative agreement with the unified model of AGNs (Antonucci 1993; Netzer 2015).

In particular, Farina et al. (2014) (and Johnson, Chen & Mulchaey 2015) characterized the cool gas contents across the line of sight of quasar host haloes as a function of projected distance and found a large amount of Mg II with  $EW > 0.3 \text{ \AA}$  extending to 200 (300) kpc from the quasars considered. The steep drop in covering fraction,  $f_C^{MgII}$ , at distances larger than 200 (300) kpc requires that this Mg II gas lies predominantly within the host halo (see fig. 4 of Farina et al. 2014 or fig. 3 of Johnson et al. 2015).

In contrast with these results, we have shown in Section 4.2 the lack of a strong Mg II absorption signal in the proximity of the quasar along the line of sight. We now measure the Mg II covering fraction,  $f_C^{MgII}$ , as a function of the velocity offset from  $z_{em}$ . This is defined as the ratio between the number of quasars showing at least one Mg II absorber within a given velocity separation of  $z_{em}$  and the total number of quasars with spectral coverage across the Mg II lines. Poissonian uncertainties are taken into account. The result is shown in Fig. 6. The frequency with which Mg II is detected in our survey is 6 per cent for absorbers with  $v_{abs} < 5000 \text{ km s}^{-1}$  and 8 per cent for those with  $5000 < v_{abs} < 10000 \text{ km s}^{-1}$ . Moreover, if we consider only absorbers with  $v_{abs} < 5000 \text{ km s}^{-1}$  and  $EW > 0.3 \text{ \AA}$ , we see that they are all related to identified DLA systems (Berg et al. 2017), probably unrelated to the quasar host galaxy. This supports our finding in P16 of a dearth of cool gas traced by C II in AALs along direct lines of sight to the quasars, in contrast with results based on projected quasar pairs (Prochaska et al. 2014; Lau et al. 2018).

The detection fraction derived in Farina et al. (2014) (or Johnson et al. 2015) cannot be compared directly with our result. Indeed, the velocity offset of each Mg II absorber detected in our survey cannot be translated directly into a physical separation from the quasar, because the redshift also includes information on its peculiar velocity. If we did that, we would derive a proper distance of the order of  $\sim 10 \text{ Mpc}$ , implying a lack of correlation between the absorption system and the quasar host galaxy. Probably, all the gas explored in those works is contained in our first bin, within  $5000 \text{ km s}^{-1}$  of  $z_{em}$ . What is relevant is that we observe a dramatically different Mg II

covering fraction at any velocity separation that is reasonable to associate with gas within the host galaxy.

#### 4.4 Importance of barycentre determination

In the previous sections, we have considered the position of the deepest component of each C IV system as the zero velocity point around which we select the regions to produce the stacked spectrum (as described in Section 3). Such barycentre selection is justified by the fact that low-ionization ions in our sample generally appear to be well-aligned with the deepest component of C IV systems that exhibit a complex velocity-component structure. Now, we explore how the stacking is affected by this choice (see also Ellison et al. 2000).

The deepest component of the C IV systems in our sample does not always coincide with the centre of their velocity profiles. The most affected systems are those for which it is not possible to discern the individual narrow components within the adopted clustering velocity (see Section 2). They are usually the strongest systems in a given velocity bin and dominate the final composite spectrum. As a consequence, the stacked absorption profiles appear slightly asymmetric (see Fig. 4). In contrast, this trend does not affect the weak systems, which we are able to consider separately from each other.

We now calculate the barycentre position of each C IV system, weighting the wavelengths with the optical depth of the line profile. Fig. A4 in the Appendix shows the results. This technique produces more symmetric absorption troughs for intermediate- and high-ionization ions. However, their profiles are broader and less representative of the width of direct individual detections. In addition, this method spreads out the signal of the low-ionization ions, making their signatures less evident and in some cases off-centred. This latter effect happens because most low-ionization ions are associated with DLA systems and their absorption profile is often asymmetric. In conclusion, selecting the barycentre of the regions to be stacked according to the minimum of each C IV system, we produce much more coherent absorption signatures.

We also note that, while the NV stacked spectrum matches the kinematic profile of the corresponding C IV, the O VI absorption trough appears more irregular and broad (see Fig. 4). NV absorptions arise predominately at the same velocity as C IV, while O VI is often significantly shifted to positive velocities, at both high and low redshift (e.g. Carswell, Schaye & Kim 2002; Lopez et al. 2007; Tripp et al. 2008; Fechner & Richter 2009). The usual interpretation of this often observed velocity shift between O VI and C IV (e.g. Reimers et al. 2001; Carswell et al. 2002; Simcoe, Sargent & Rauch 2002) is that the lines do not arise from the same volume. However, the origin of the shift remains uncertain.

In summary, we find that the NV features in our sample are well-aligned with C IV, implying that both species arise from the same gas phase, whereas velocity offsets between C IV and O VI centroids may contribute to producing a broader stacked profile compared with other species. We will discuss the possible origin of NV and O VI more extensively in Section 5.1.

## 5 DISCUSSION

In this article, we stack 100 quasar spectra in the rest-frame of C IV absorbers detected in the dataset of the XQ-100 Legacy Survey, to

examine the typical strength of N V and other lines in the vicinity of quasars compared with intervening gas. The combination of moderate resolution, high S/N and wide wavelength coverage of our survey have allowed us to build composite spectra at redshifts 2.55–4.73 and at the same time explore a wide range of strong and weak NALs.

From now on, we refer to the top panels of Fig. 5 (panels a and e) to describe the associated region for strong and weak systems, respectively. On the other hand, the bottom panels (panels d and h) characterize intervening gas. Fig. 5(d) and (h) correspond to a velocity offset from  $z_{\text{em}}$  ( $10\,000 < v_{\text{abs}} < 35\,000 \text{ km s}^{-1}$ ) that includes both of the smaller bins explored in the two upper panels and is large enough to allow the investigated ions to produce measurable absorptions. Besides this, we are confident that in Fig. 5(d) and (h) only intervening systems are selected, because this velocity bin does not encompass the excess of NALs within  $10\,000 \text{ km s}^{-1}$  of  $z_{\text{em}}$  found in P16 (see Fig. A1 for more details). DLAs have been excluded from the stacking, since they represent a special class of systems.

AALs are characterized by higher ionization states than intervening absorbers. Indeed, we can see in Fig. 5 that N V exhibits a strong absorption signal only within  $5000 \text{ km s}^{-1}$  of  $z_{\text{em}}$ . This absorption trough is much stronger if C IV systems with  $N(\text{C IV}) > 10^{14} \text{ cm}^{-2}$  are used to build the composite spectrum. We draw attention to the fact that O VI is detected in the proximity of the quasar, as well as in the intervening gas. This is not surprising, since O VI absorption is observed in a wide range of astrophysical environments (see Fox 2011 for a review). However, the O VI/C IV ratio is higher in AALs. Fig. 5 also shows that Si IV is detected both in the proximity of the quasar and in the intervening gas. Nevertheless, it is much weaker close to the quasar, where the gas is more easily ionized, and it is thus reasonable to expect that a smaller fraction of silicon is in the form of Si IV. We note that the Si III signal increases moving further from the quasar and that the Si IV/Si III and Si IV/C IV ratios suggest lower ionization in intervening systems with respect to associated ones. This is true for the composite spectra obtained selecting both weak and strong C IV systems. AALs are also characterized by the absence of low-ionization ions. They are found, instead, at large velocity separation from  $z_{\text{em}}$ , but only associated with the strongest C IV systems in the sample (i.e.  $N(\text{C IV}) > 10^{14} \text{ cm}^{-2}$ ). Indeed, low-ionization metal transitions, such as Mg II, C II and Si II, are mostly found at  $N(\text{H I}) \geq 10^{16} \text{ cm}^{-2}$  (e.g. Farina et al. 2014).

Fig. 5 clearly shows that the gas in the proximity of the quasar exhibits a considerably different ionization state with respect to the intervening gas. In order to illustrate how the absorption-line strengths of the explored ions vary as a function of different physical conditions, we use the CLOUDY software package (v17.00; Ferland et al. 2017) to run ionization models.

A photoionized plasma is characterized by the ionization parameter,  $U = Q_{\text{H}}/4\pi R^2 n_{\text{H}} c$ , where  $Q_{\text{H}}$  is the source emission rate of hydrogen ionizing photons,  $R$  is the distance from the central source,  $n_{\text{H}}$  is the hydrogen density and  $c$  is the speed of light. The top panel of Fig. 7 exhibits how the column densities of several ions within a cloud of total column density  $\log N(\text{H}) = 20 \text{ cm}^{-2}$  vary as a function of  $U$ . In this model, the gas is assumed to be photoionized only by the radiation field of the quasar. The adopted bolometric luminosity of the quasar is  $L = 10^{47} \text{ erg s}^{-1}$ , representative of the XQ-100 sample (see P16). We consider a metallicity  $\log Z = -1.0$ , with solar relative abundances. We note that, close to the quasar (high values of  $U$ ), the intense and hard radiation field eliminates low ions and allows nitrogen and oxygen to be highly ionized. Mov-

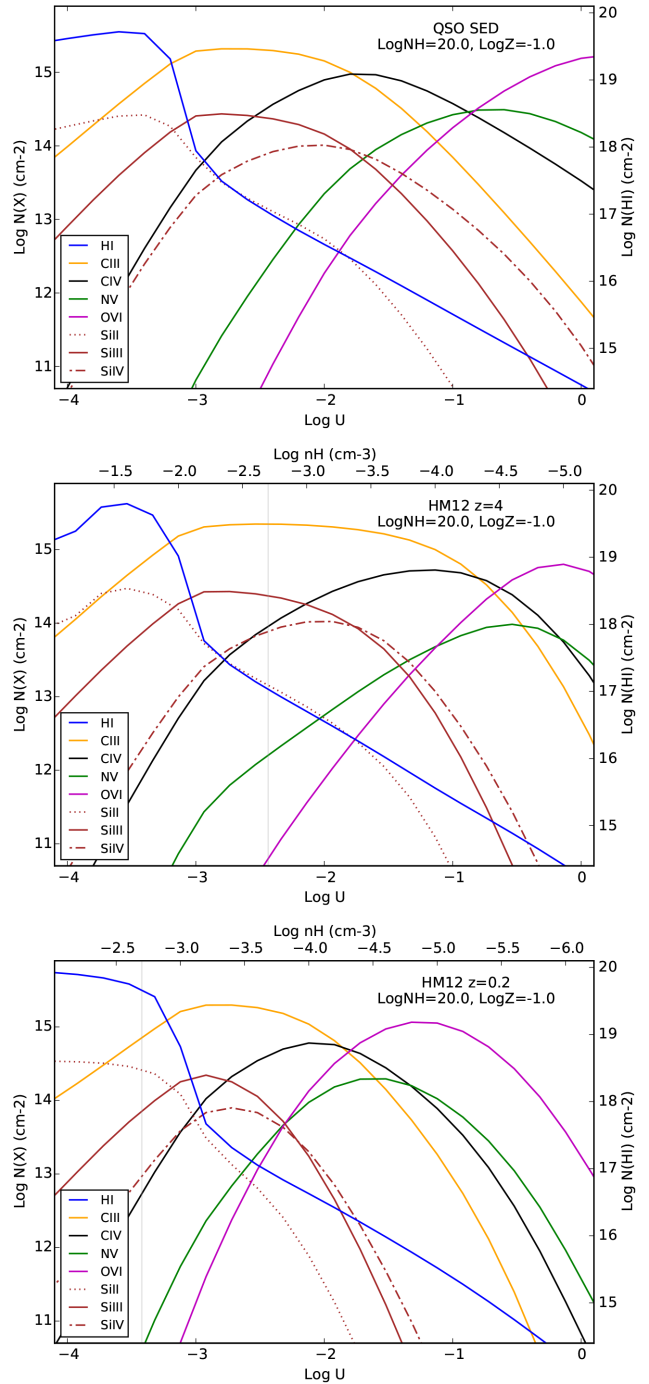


**Figure 7.** CLOUDY-predicted column densities as a function of the ionization parameter  $U$ , for a cloud of total column density  $\log(N_{\text{H}}) = 20 \text{ cm}^{-2}$ . The metallicity of the cloud is  $\log Z = -1.0$  with solar relative abundances.  $N(\text{H I})$  is shown by the bold blue curve and axis labels on the right. Top panel: the gas is assumed to be photoionized by a quasar spectral energy distribution. Middle and bottom panels: the gas is assumed to be photoionized by the UV background radiation (Haardt & Madau 2012) at  $z = 4$  (middle panel) and  $z = 0.2$  (bottom panel).

ing further from the quasar, the decrease of  $U$  produces a drop in the N V and O VI absorption signal and the appearance of low ions.

Fig. 8 illustrates this trend even better, showing how the column densities of the same ions vary as a function of the distance,  $R$ , from a quasar at  $z = 4$  (properties of the cloud as in Fig. 7). The gas

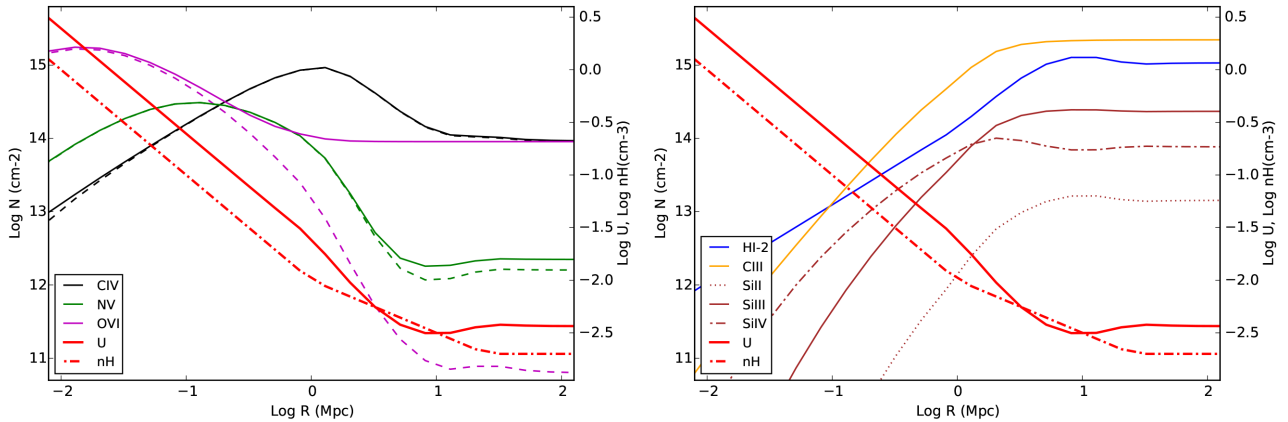


**Figure 8.** CLOUDY-predicted column densities as a function of the distance,  $R$ , from a quasar at  $z = 4$ . The metallicity of the cloud is  $\log Z = -1.0$  with solar relative abundances and the total column density is  $\log(N_{\text{H}}) = 20$ . The gas is modelled as a uniform slab in thermal and ionization equilibrium and is assumed to be photoionized by the radiation field of a quasar with bolometric luminosity  $L = 10^{47}$  erg  $\text{s}^{-1}$  and the UV background radiation (Haardt & Madau 2012). We also add a thermal gas component with  $\log T = 5.5$ . The solid curves show the sum of the two contributions, while the dashed ones show just the photoionized component. The ions in the right panel are not affected by the thermal component. The HI column density, labeled ‘HI-2’, is plotted as  $\log N(\text{HI}) - 2.0$  to fit on the plot. The densities of the cloud and the  $U$  parameters at each  $R$  are shown by the dot-dashed and bold red curves, respectively, and the axis labels on the right. Left: C IV, N V and O VI column densities. Right: low-ion column densities.

is assumed to be photoionized by the radiation field of the quasar and the UV background (Haardt & Madau 2012). We also add a thermal gas component with  $\log T = 5.5$  to mimic the effect of collisionally ionized gas. The dashed curves show the photoionized component, while the solid ones represent the sum of the two contributions.

Let us focus on the photoionized component first. We can see in the left panel of Fig. 8 that N V and O VI (and slightly C IV) drop with distance from the quasar, because the gas is subjected to lower values of  $U$  (it corresponds to moving to the left in the top panel of Fig. 7). Those ions signal would continue to decrease, except that at large  $R$  they hit a floor determined by the UV background. Fig. A2 in the Appendix shows that the UV background at  $z = 4$  starts to dominate the ionizing continuum ( $> 13.6\text{eV}$ ) at  $R \gtrsim 3$  Mpc, but its spectral energy distribution (SED) is strongly shaped by deep edges due to H I and He II ionization. In particular, the C III edge is at lower energies than the He II one, so the UV background radiation at  $z = 4$  can produce C IV, but it cannot produce much O VI and manages even less N V. The right panel of Fig. 8 shows how, moving away from the quasar, the decrease of  $U$  allows the low-ion absorption signal to rise.

The trends illustrated in Fig. 8 give a natural explanation for the increase in Si IV/C IV and Si III/Si IV ratios we see in Fig. 5 moving towards gas at large separation from the quasar. The substantial difference in the N V/C IV ratio between AAL and intervening systems is also well described. However, if the drop of  $U$  were the only factor in play, we should detect a much weaker O VI signal far from the  $z_{\text{em}}$  in our composite spectra. Indeed, the N V ionization potential is in between those of C IV and O VI and we can see in Fig. 5 that the N V signal drops moving away from the quasar, while the O VI/C IV ratio is not subject to a change consistent with that of N V. This trend can have multiple interpretations.

One possibility is that O VI traces another phase of the absorbing gas, independently from the environment, and it has a different mechanism of production with respect to N V, so the change in ionization radiation at large distance from the quasar affects only the N V signal. This is unlikely, since O VI is often found to be photoionized (e.g. Bergeron et al. 2002; Reimers et al. 2006; Fechner

& Richter 2009). It is also possible that O VI is photoionized in the proximity of the quasar and has a different channel of production in other environments.

Fig. 8 clearly illustrates that a thermal gas component with  $\log T = 5.5$  increases  $N(\text{OVI})$  significantly at large  $R$  (magenta curves), but it contributes little to  $N(\text{Nv})$  (green) and negligibly to  $N(\text{CIV})$  (black). This model suggests that, moving further from the quasar, the change in the  $U$  parameter causes a drop in both N V and O VI. The fact that we see an O VI signal in our composite spectra even at large velocity offsets from  $z_{\text{em}}$  can be explained by an additional thermal gas component.

The right panel of Fig. 5 shows that lower  $N(\text{CIV})$  systems have much higher C III/C IV than those with high  $N(\text{CIV})$ . Therefore, on selecting weak C IV absorbers we do not simply find lower total column densities. We also find systems with lower ionization. However, this trend cannot be explained only by changing  $U$ , because the strong C III and larger C III/C IV ratios are not (clearly) accompanied by stronger absorption in other lower ions. All of these absorbers can have a range of  $n_{\text{H}}$ , which means a range in  $U$  values. So, from a distribution of absorbers, systems with weak C IV NALs and small C IV/C III ratios might have relatively less low  $n_{\text{H}}$ , high  $U$  gas (not simply lower  $U$  overall).

### 5.1 N v and OVI as diagnostics of ionization mechanisms

Conclusions regarding the origin and fate of the CGM are linked to the assumptions one makes about the physical processes that determine its ionization state. Successful models of the CGM must account for the full suite of observations available and combine together the two dominant gas phases, typically described as a cool  $\sim 10^4$  K and a warm  $\sim 3 \times 10^5$  K phase. In this context, the presence or absence of N V and O VI in quasar absorption systems may provide crucial information for understanding the physical conditions of the absorbing gas. N V and O VI require 77.5 (97.9) and 113.9 (138.1) eV to be created via photoionization (to be destroyed), respectively, and their abundance peaks at  $2 \times 10^5$  and  $3 \times 10^5$  K for collisionally ionized gas (Gnat & Sternberg 2007).

Lu & Savage (1993) performed a search for N V and O VI absorption based on a composite spectrum method. To this aim they

exploited a total of 73 intervening C IV systems (with mean redshift  $\langle z \rangle = 2.76$ ) identified in 36 spectra from the survey by Sargent, Steidel & Boksenberg (1989). The results of this study may apply to relatively strong systems, since only C IV absorbers with rest-frame equivalent width  $\geq 0.3 \text{ \AA}$  can be detected in those spectra. This work provided the first firm evidence for the presence of O VI absorption in intervening quasar metal line systems, while the N V doublet was not detected. This agrees with what we find in our composite spectrum obtained selecting only strong C IV absorbers. They estimated the ratio  $N(\text{OVI})/N(\text{NV})$  to be  $\geq 4.4$ , which, for collisionally ionized gas in thermal equilibrium with a solar ratio of oxygen to nitrogen, implies a gas temperature  $T \geq 2.5 \times 10^5 \text{ K}$ .

More recently, many detailed studies have been carried out on an absorber-by-absorber basis in quasar spectra that trace low-density foreground gas in the IGM and galaxy haloes. These studies have shown that the ionization mechanisms of high-ionization species like O VI and N V are complex and vary over a wide range of environments. Line diagnostics from low, intermediate, and high ions sometimes support a similar, photoionized origin for O VI, N V and low-ionization state gas (e.g. Tripp et al. 2008; Muzahid et al. 2015) and sometimes require O VI to be ionized by collisions of electrons with ions in a  $\sim 3 \times 10^5 \text{ K}$  plasma (e.g. Tumlinson et al. 2005; Fox et al. 2009; Wakker et al. 2012; Meiring et al. 2013).

Recently, the work by Werk et al. (2016) reported on quasars probing sight lines near 24 star-forming galaxies with  $L \approx L^*$  at  $z = 0.2$  from the COS–Halos survey (Werk et al. 2013; Tumlinson et al. 2013), which exhibit positive detections of O VI in their inner CGM. Of the galaxies analysed, only three have positive detections of N V. They also argue about the possibility that N V does not trace the same gas phase as O VI, since they show different velocity profiles. However, a N V upper limit can impose meaningful constraints in both photoionized and collisionally ionized gas models. For example, the upper limits on  $\log N(\text{NV})/N(\text{OVI}) \sim -1$  strongly rule out most photoionization models, both in and out of equilibrium. Bordoloi et al. (2017) claim that most of the observed COS–Halos O VI absorption-line systems can be explained as collisionally ionized gas radiatively cooling behind a shock or other type of radiatively cooling flow. Their model predicts typical N V column densities to be an order of magnitude smaller than the O VI ones at similar cooling velocities. Therefore, most of the COS–Halos N V systems associated with O VI absorption would reside below the detection threshold, consistent with N V non-detection for the majority of the COS–Halos O VI. In the context of a multiphase CGM, however, this scenario does not take into account the constraints on the N V signal coming from photoionization models based on low and intermediate ions.

Fig. 7 shows the CLOUDY-predicted column densities of several ions as a function of the ionization parameter  $U$ , for a cloud of total column density  $\log(N_{\text{H}}) = 20 \text{ cm}^{-2}$ , at  $z = 4$  (middle panel) and  $z = 0.2$  (bottom panel). We model a cloud with the same parameters as in Fig. 8, to investigate how the picture described at large separation from the quasar changes with redshift. The vertical grey line in the middle panel marks  $U$  and  $n_{\text{H}}$  reached at large distance in Fig. 8. We note that, considering the same  $U$  parameter, the Haardt & Madau (2012) spectrum produces more N V and O VI at low  $z$ . Fig. A2 in the Appendix shows that the UV background flux at energies from  $\sim 13.6$  to  $\sim 45 \text{ eV}$  is weaker at  $z = 0.2$  by 0.98 dex compared with  $z = 4$ . However, for any given density, it produces  $\sim 10$  times lower  $U$  at  $z = 0.2$  than at  $z = 4$ , but more N V and O VI, due to the harder continuum shape around the energies that create those ions. Single-phase photoionization models fail in explaining the range of  $N(\text{NV})/N(\text{OVI})$  reported by studies at low  $z$  (e.g. the COS–

Halos survey). As discussed in Werk et al. (2016), the observed  $\log N(\text{NV})/N(\text{OVI}) \sim -1$  would require very low gas density for the CGM with  $U \geq -1$  (see the bottom panel of Fig. 7). However, depending on the physical condition of the cloud, the N V signal produced by photoionization can be an important contribution to the total strength of the absorbing line. Therefore, before using N V non-detection to derive a limit on the gas temperature, one can exploit the constraints from low and intermediate ions to predict the N V absorption produced by UV background radiation.

The details of the mechanisms that ionize the absorbing gas can rapidly become complex if non-equilibrium processes are occurring and/or if there is a combination of photoionization and collisional ionization (see Savage et al. 2014, for a recent review). Among the models proposed to reproduce the intermediate- and high-ion states (e.g. C IV, N V, O VI) are (1) time-variable radiation fields from AGNs coupled with non-equilibrium ionization effects (Segers et al. 2017; Oppenheimer et al. ), (2) radiative cooling flows (Bordoloi et al. 2017; McQuinn & Werk 2018), (3) formation in fast shocks (Gnat & Sternberg 2009) or (4) formation within thermally conductive interfaces (Gnat, Sternberg & McKee 2010; Armillotta et al. 2017).

We have shown that it is possible that N V is photoionized in environments where O VI is mostly collisionally ionized, but being weak it is hard to detect. We have also demonstrated that the observed differences in the N V/C IV ratio between AALs and intervening systems can be explained naturally by ionization effects. However, another factor that can contribute in making the intervening N V signal weaker than already expected is that these absorbers can trace gas in regions with lower metallicity or subsolar  $N/\alpha$  relative abundance. N V absorptions are largely identified in proximity to bright quasars along the line of sight (e.g. Misawa et al. 2007; Nestor, Hamann & Rodriguez Hidalgo 2008; Ganguly et al. 2013; P16; Chen & Pan 2017). Quasars are generally metal-rich and about solar  $[\text{N}/\text{H}]$  has been measured in associated systems (Petitjean, Rauch & Carswell 1994; Dietrich et al. 2003; D’Odorico et al. 2004; Ganguly et al. 2006; Schaye, Carswell & Kim 2007), making N V easily detectable in proximate absorbers. Nitrogen is rarely detected in optically thin (i.e.  $N(\text{HI}) \lesssim 10^{17} \text{ cm}^{-2}$ ) intergalactic absorption systems. In the IGM, the metallicity and therefore the nitrogen content is lower, thus N V features are expected to be weak (Fechner & Richter 2009).

Fechner & Richter (2009) find that the  $[\text{N}/\alpha]$  abundance in intervening systems is clearly subsolar, with a median  $[\text{N}/\alpha] = -0.58$  and values down to  $\sim -1.8$ . Observations have shown that the N/O ratio can diminish the moving outwards of disc galaxies as a function of galactocentric distance and stellar mass (e.g. Belfiore et al. 2017). This result is supported by chemical evolution models included within cosmological hydrodynamical simulations (Vincenzo & Kobayashi 2018a,b). ‘Down the barrel’ observations give us access to gas originating at small distances from the centre of the quasar host galaxy (e.g. Wu et al. 2010). In contrast, the absorption systems identified in works based on projected pairs usually have impact parameters from tens to hundreds of kpc from the  $z_{\text{em}}$  of the background target, so they trace gas in the outskirts of galaxies possibly characterized by a lower N/O ratio.

## 6 CONCLUSIONS

In this work, we present new measurements of metal NALs made using composite quasar spectra. Our sample includes 100 individual lines of sight from the XQ-100 Legacy survey, at emission redshift  $z_{\text{em}} = 3.5\text{--}4.72$ . To build the stacking spectra, we start from a large

number ( $\sim 1000$ ) of C IV absorption systems identified in P16, covering the redshift range  $2.55 < z_{\text{abs}} < 4.73$ . The main goal of our analysis is to investigate the N V absorption signal at large velocity separations from  $z_{\text{em}}$ . This study complements our previous work on N V and tests the robustness of the use of N V as a criterion to select intrinsic NALs. We also characterize the ionization state of the gas, both near and at great distance from the quasar. Our primary results are as follows.

(1) We show the absence of a statistically significant intervening N V absorption signal along the line of sight of background quasars. Indeed, the N V exhibits a strong absorption trough only within  $5000 \text{ km s}^{-1}$  of  $z_{\text{em}}$ . This feature is much stronger ( $\sim 15\sigma$  confidence level) if C IV systems with  $N(\text{C IV}) > 10^{14} \text{ cm}^{-2}$  are considered to build the composite spectrum. This result supports our previous claim (see P16) that N V is an excellent statistical tool for identifying intrinsic systems.

(2) We use photoionization models to show that, in a scenario where associated systems are photoionized by a quasar, the ionization parameter is expected to drop dramatically with distance from the continuum source. This is the main reason for intervening N V systems being weaker than associated ones. Another possible contribution to this trend is a lower metallicity or N/O abundance.

(3) The gas close to the continuum source ( $v_{\text{abs}} < 5000 \text{ km s}^{-1}$ ) exhibits a different ionization state with respect to the intervening one. Moving further from the quasar, we can appreciate the appearance of the low ions associated with the strongest systems in the sample ( $N(\text{C IV}) > 10^{14} \text{ cm}^{-2}$ ) and the drop in the N V absorption signal. In contrast, the O VI NAL is detected even at large velocity shifts from  $z_{\text{em}}$ . We also note that O VI and C IV do not exhibit a change in their absorption signal in line with the decrease of the N V signal. We run photoionization models that describe these trends well (see Fig. 8). We use these models to illustrate that a drop in the  $U$  parameter cannot be the only element to explain the data and that an additional thermal component ( $T \sim 3 \times 10^5 \text{ K}$ ) can produce the O VI absorption we detect at large distance from the quasar. We show how it is possible that N V is photoionized in environments where O VI is mostly collisionally ionized, but, being weak, this can be challenging to detect.

(4) We verify the deficiency of cool gas, as traced by low ions and in particular by Mg II, in the proximity of the quasar. This finding is in agreement with the dearth of C II NALs (as shown in P16) and confirms that the gas in the proximity of the quasar along the line of sight has a different ionization state with respect to gas in the transverse direction (e.g. Farina et al. 2014; Prochaska et al. 2014).

## ACKNOWLEDGEMENTS

The XQ-100 team is indebted to the European Southern Observatory (ESO) staff for support through the Large Program execution process.

## REFERENCES

- Antonucci R., 1993, *ARA&A*, 31, 473
- Armillotta L., Fraternali F., Werk J. K., Prochaska J. X., Marinacci F., 2017, *MNRAS*, 470, 114
- Belfiore F. et al., 2017, *MNRAS*, 469, 151
- Berg T. A. M. et al., 2017, *MNRAS*, 464, L56
- Berg T. A. M., Ellison S. L., Tumlinson J., Oppenheimer B. D., Horton R., Bordoloi R., Schaye J., 2018, *MNRAS*, 478, 3890
- Bergeron J., Aracil B., Petitjean P., Pichon C., 2002, *A&A*, 396, L11
- Bordoloi R., Wagner A. Y., Heckman T. M., Norman C. A., 2017, *ApJ*, 848, 122
- Bowen D. V. et al., 2006, *ApJ*, 645, L105
- Carswell B., Schaye J., Kim T.-S., 2002, *ApJ*, 578, 43
- Chen Z.-F., Pan D.-S., 2017, *ApJ*, 848, 79
- Chen Z.-F., Huang W.-R., Pang T.-T., Huang H.-Y., Pan D.-S., Yao M., Nong W.-J., Lu M.-M., 2018, *ApJS*, 235, 11
- Cowie L. L., Songaila A., Kim T.-S., Hu E. M., 1995, *AJ*, 109, 1522
- Crenshaw D. M., Kraemer S. B., Boggess A., Maran S. P., Mushotzky R. F., Wu C.-C., 1999, *ApJ*, 516, 750
- D’Odorico V., Cristiani S., Romano D., Granato G. L., Danese L., 2004, *MNRAS*, 351, 976
- D’Odorico V. et al., 2016, *MNRAS*, 463, 2690
- Di Matteo T., Springel V., Hernquist L., 2005, *Nature*, 433, 604
- Dietrich M., Appenzeller I., Hamann F., Heidt J., Jäger K., Vestergaard M., Wagner S. J., 2003, *A&A*, 398, 891
- Ellison S. L., Songaila A., Schaye J., Pettini M., 2000, *AJ*, 120, 1175
- Farina E. P., Falomo R., Decarli R., Treves A., Kotilainen J. K., 2013, *MNRAS*, 429, 1267
- Farina E. P., Falomo R., Scarpa R., Decarli R., Treves A., Kotilainen J. K., 2014, *MNRAS*, 441, 886
- Faucher-Giguère C.-A., Kereš D., 2011, *MNRAS*, 412, L118
- Fechner C., Richter P., 2009, *A&A*, 496, 31
- Ferland G. J. et al., 2017, *RMxAA*, 53, 385
- Fox A. J., 2011, *ApJ*, 730, 58
- Fox A. J., Prochaska J. X., Ledoux C., Petitjean P., Wolfe A. M., Srianand R., 2009, *A&A*, 503, 731
- Fumagalli M., Prochaska J. X., Kasen D., Dekel A., Ceverino D., Primack J. R., 2011, *MNRAS*, 418, 1796
- Ganguly R., Bond N. A., Charlton J. C., Eracleous M., Brandt W. N., Churchill C. W., 2001, *ApJ*, 549, 133
- Ganguly R., Sembach K. R., Tripp T. M., Savage B. D., Wakker B. P., 2006, *ApJ*, 645, 868
- Ganguly R. et al., 2013, *MNRAS*, 435, 1233
- Gnat O., Sternberg A., 2007, *ApJS*, 168, 213
- Gnat O., Sternberg A., 2009, *ApJ*, 693, 1514
- Gnat O., Sternberg A., McKee C. F., 2010, *ApJ*, 718, 1315
- Granato G. L., De Zotti G., Silva L., Bressan A., Danese L., 2004, *ApJ*, 600, 580
- Haardt F., Madau P., 2012, *ApJ*, 746, 125
- Hamann F., Beaver E. A., Cohen R. D., Junkkarinen V., Lyons R. W., Burbidge E. M., 1997, *ApJ*, 488, 155
- Hennawi J. F., Prochaska J. X., 2013, *ApJ*, 766, 58
- Hennawi J. F. et al., 2006, *ApJ*, 651, 61
- Hopkins P. F., Elvis M., 2010, *MNRAS*, 401, 7
- Hopkins P. F., Torrey P., Faucher-Giguère C.-A., Quataert E., Murray N., 2016, *MNRAS*, 458, 816
- Johnson S. D., Chen H.-W., Mulchaey J. S., 2015, *MNRAS*, 452, 2553
- Kim T.-S., Carswell R. F., Mongardi C., Partl A. M., Mückel J. P., Barai P., Cristiani S., 2016, *MNRAS*, 457, 2005
- King A., 2003, *ApJ*, 596, L27
- Kirkman D. et al., 2005, *MNRAS*, 360, 1373
- Lau M. W., Prochaska J. X., Hennawi J. F., 2016, *ApJS*, 226, 25
- Lau M. W., Prochaska J. X., Hennawi J. F., 2018, *ApJ*, 857, 126
- Lopez S., Ellison S., D’Odorico S., Kim T.-S., 2007, *A&A*, 469, 61
- López S. et al., 2016, *A&A*, 594, A91
- Lu L., Savage B. D., 1993, *ApJ*, 403, 127
- McConnell N. J., Ma C.-P., 2013, *ApJ*, 764, 184
- McQuinn M., Werk J. K., 2018, *ApJ*, 852, 33
- Meiring J. D., Tripp T. M., Werk J. K., Howk J. C., Jenkins E. B., Prochaska J. X., Lehner N., Sembach K. R., 2013, *ApJ*, 767, 49
- Misawa T., Charlton J. C., Eracleous M., Ganguly R., Tytler D., Kirkman D., Suzuki N., Lubin D., 2007, *ApJS*, 171, 1
- Morton D. C., 2003, *ApJS*, 149, 205
- Muzahid S., Kacprzak G. G., Churchill C. W., Charlton J. C., Nielsen N. M., Mathes N. L., Trujillo-Gomez S., 2015, *ApJ*, 811, 132
- Nestor D., Hamann F., Rodriguez Hidalgo P., 2008, *MNRAS*, 386, 2055
- Netzer H., 2015, *ARA&A*, 53, 365
- Perrotta S. et al., 2016, *MNRAS*, 462, 3285
- Petitjean P., Rauch M., Carswell R. F., 1994, *A&A*, 291, 29

- Pieri M. M., Frank S., Weinberg D. H., Mathur S., York D. G., 2010, *ApJ*, 724, L69
- Pieri M. M. et al., 2014, *MNRAS*, 441, 1718
- Planck Collaboration et al., 2014, *A&A*, 571, A16
- Prochaska J. X., Hennawi J. F., 2009, *ApJ*, 690, 1558
- Prochaska J. X., O'Meara J. M., Worseck G., 2010, *ApJ*, 718, 392
- Prochaska J. X., Lau M. W., Hennawi J. F., 2014, *ApJ*, 796, 140
- Reimers D., Baade R., Hagen H.-J., Lopez S., 2001, *A&A*, 374, 871
- Reimers D., Agafonova I. I., Levshakov S. A., Hagen H.-J., Fechner C., Tytler D., Kirkman D., Lopez S., 2006, *A&A*, 449, 9
- Sánchez-Ramírez R. et al., 2016, *MNRAS*, 456, 4488
- Sargent W. L. W., Steidel C. C., Boksenberg A., 1989, *ApJS*, 69, 703
- Savage B. D., Kim T.-S., Wakker B. P., Keeney B., Shull J. M., Stocke J. T., Green J. C., 2014, *ApJS*, 212, 8
- Scannapieco E., Oh S. P., 2004, *ApJ*, 608, 62
- Schaye J., Aguirre A., Kim T.-S., Theuns T., Rauch M., Sargent W. L. W., 2003, *ApJ*, 596, 768
- Schaye J., Carswell R. F., Kim T.-S., 2007, *MNRAS*, 379, 1169
- Segers M. C., Oppenheimer B. D., Schaye J., Richings A. J., 2017, *MNRAS*, 471, 1026
- Shen Y., Ménard B., 2012, *ApJ*, 748, 131
- Simcoe R. A., Sargent W. L. W., Rauch M., 2002, *ApJ*, 578, 737
- Songaila A., 1998, *AJ*, 115, 2184
- Tripp T. M., Sembach K. R., Bowen D. V., Savage B. D., Jenkins E. B., Lehner N., Richter P., 2008, *ApJS*, 177, 39
- Tumlinson J., Shull J. M., Giroux M. L., Stocke J. T., 2005, *ApJ*, 620, 95
- Tumlinson J. et al., 2013, *ApJ*, 777, 59
- Vernet J. et al., 2011, *A&A*, 536, A105
- Vestergaard M., 2003, *ApJ*, 599, 116
- Vincenzo F., Kobayashi C., 2018a, *MNRAS*, 478, 155
- Vincenzo F., Kobayashi C., 2018b, *A&A*, 610, L16
- Wakker B. P., Savage B. D., Fox A. J., Benjamin R. A., Shapiro P. R., 2012, *ApJ*, 749, 157
- Weinberger R. et al., 2017, *MNRAS*, 465, 3291
- Werk J. K., Prochaska J. X., Thom C., Tumlinson J., Tripp T. M., O'Meara J. M., Peeples M. S., 2013, *ApJS*, 204, 17
- Werk J. K. et al., 2016, *ApJ*, 833, 54
- Wu J., Charlton J. C., Misawa T., Eracleous M., Ganguly R., 2010, *ApJ*, 722, 997

## APPENDIX A

The left panels of Fig. A1 show the rest-frame equivalent widths of metal species measured in the composite spectrum based on C IV systems with  $N(\text{C IV}) \geq 10^{14} \text{ cm}^{-2}$  and  $5000 < v_{\text{abs}} < 10\,000 \text{ km s}^{-1}$  (panel b), compared with results for AAL and intervening systems (panels a and c), already presented in Fig. 5. The right panels are the same as the left panels, but in this case  $N(\text{C IV}) < 10^{14} \text{ cm}^{-2}$  is considered as a threshold for the stacking.  $5000 < v_{\text{abs}} < 10\,000 \text{ km s}^{-1}$  is a particular velocity bin in our study. In P16 we find that the C IV sample exhibits a statistically significant excess ( $\sim 8\sigma$ ) within  $10\,000 \text{ km s}^{-1}$  of  $z_{\text{em}}$  with respect to the random occurrence of NALs, which is especially evident for lines with  $\text{EW} < 0.2 \text{ \AA}$ . These latter lines more or less correspond to the weak systems in the current study. The excess extends to larger velocities than the classical associated region, is not an effect of NAL redshift evolution and does not show a significant dependence on the quasar bolometric luminosity.

We note that the systems in the  $5000 < v_{\text{abs}} < 10\,000 \text{ km s}^{-1}$  bin exhibit some of the properties of the associated systems and at the same time show some characteristics of the intervening ones. Let us focus on the strong systems first. Fig. A1(b) shows that the C IV/Si IV and C IV/Si III ratios are close to those of the AALs (Fig. A1a), but O VI/C IV and N V/C IV ratios are in line with those of the intervening gas (Fig. A1c). In addition, we only measure upper limits for the low ions, in agreement with gas in the proximity of the quasar. If we consider weak systems, Fig. A1(f) shows a smaller C IV/Si III ratio like the intervening gas, but a larger value of the O VI absorption like the AALs.

Fig. A1(b) and (f) seem to represent a ‘transition’ region between associated and intervening systems. The EWs shown in those bins are produced by averaging together absorbers physically connected with the quasar host galaxy and its halo and spurious intervening systems. This is the main reason why we excluded this bin from our stacking analysis.

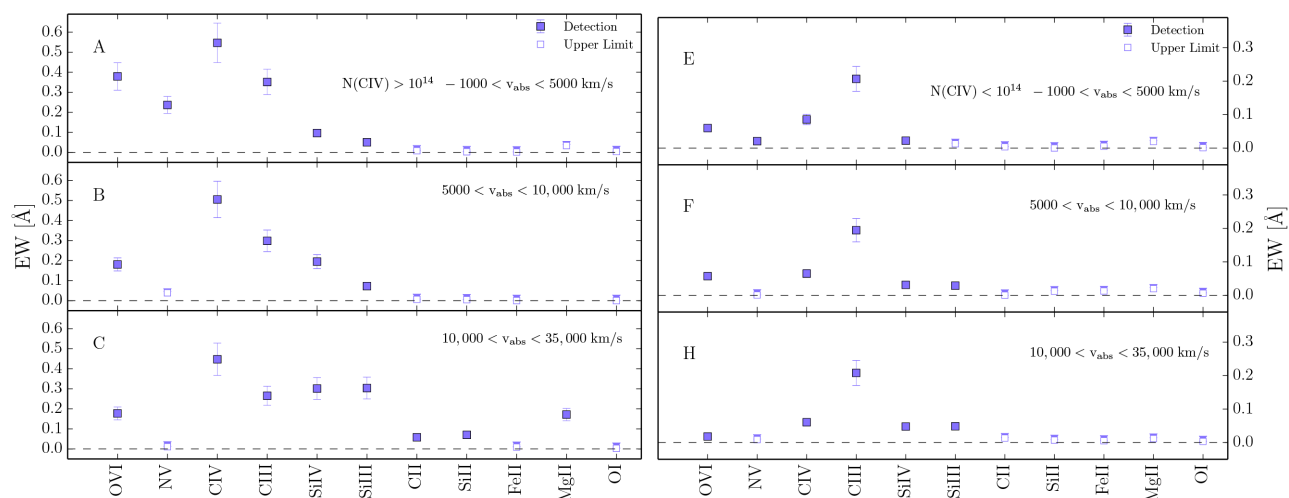


**Figure A1.** Left: equivalent widths of metal species measured in order of decreasing ionization potential for composite spectra based on C IV systems with  $N(\text{C IV}) \geq 10^{14} \text{ cm}^{-2}$ . Each panel displays the velocity offset from  $z_{\text{em}}$ . C IV DLAs have been excluded from the stacking. Right: same as for the left panels, but in this case  $N(\text{C IV}) < 10^{14} \text{ cm}^{-2}$  is considered as the threshold for the stacking. The EW refers only to the strongest member of the doublets. Error bars are  $1\sigma$  and are estimated by bootstrapping the data using 1000 realizations.

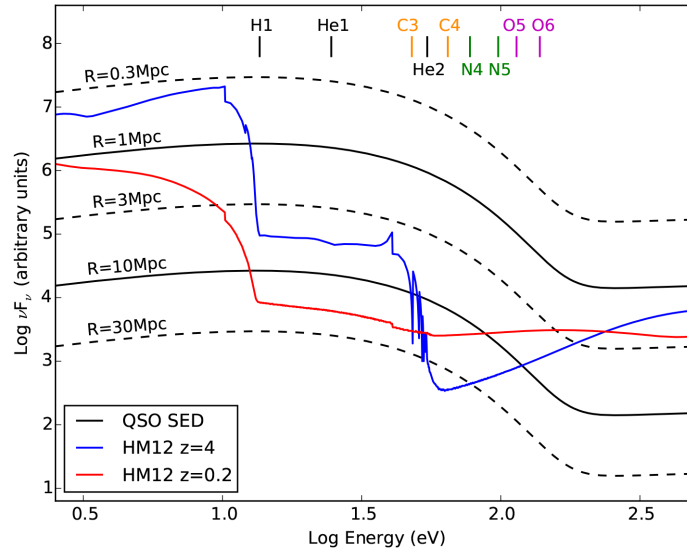


**Figure A2.** UV background (Haardt & Madau 2012) spectral energy distribution (SED) at  $z = 4$  and  $z = 0.2$ , and quasar SED scaled to different distances from the quasar. The tick marks along the top mark the ionization energies of some ions important for the discussion.

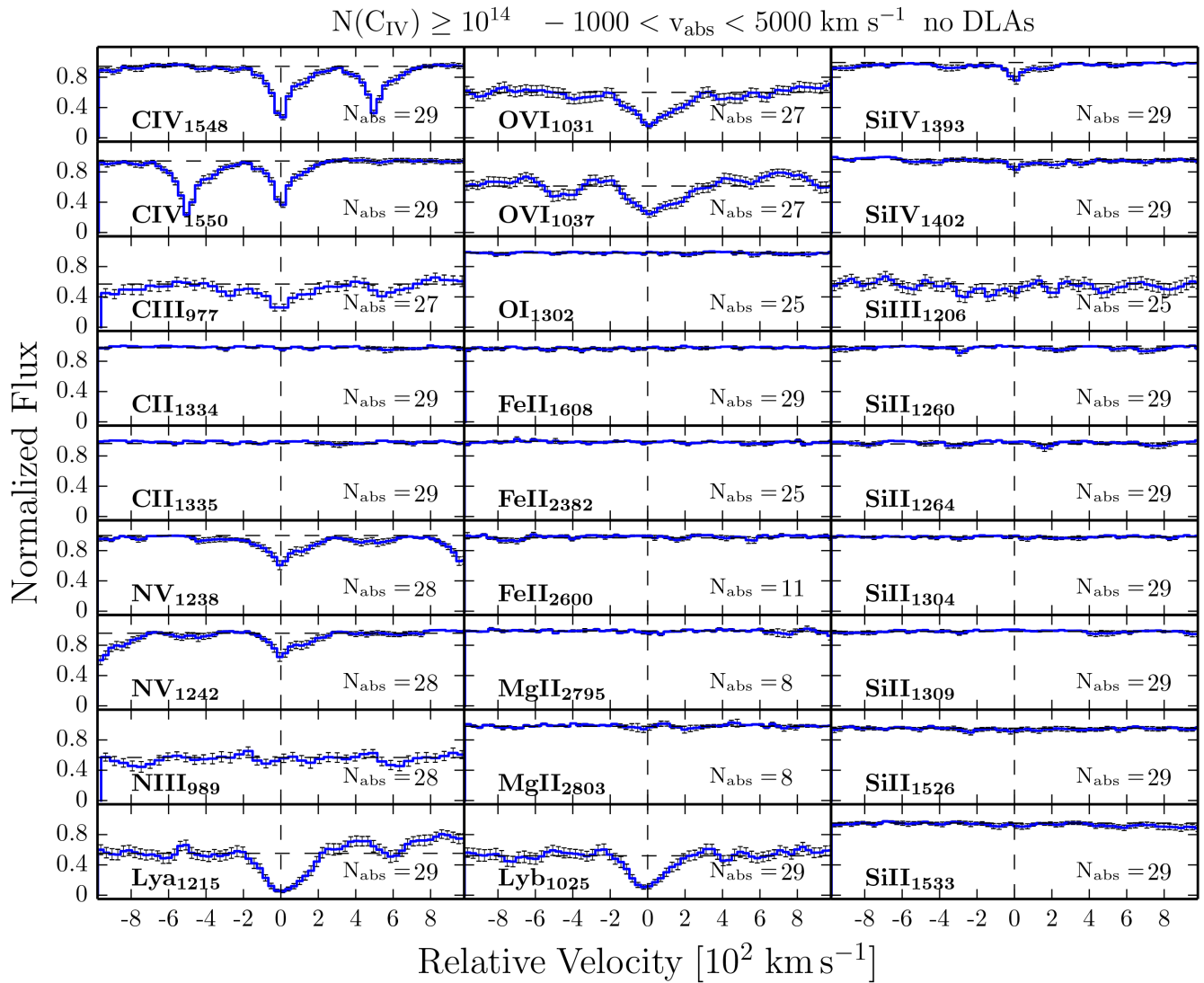


**Figure A3.** Composite spectra for the ions studied in this work, based on the C IV systems with  $N(\text{CIV}) \geq 10^{14} \text{ cm}^{-2}$  and  $-1000 < v_{\text{abs}} < 5000 \text{ km s}^{-1}$ . C IV DLAs are excluded from the stacking. Every panel reports the number of absorbers considered to build the stacked spectrum. The error bars are  $1\sigma$  and are estimated by bootstrapping the data using 1000 realizations.

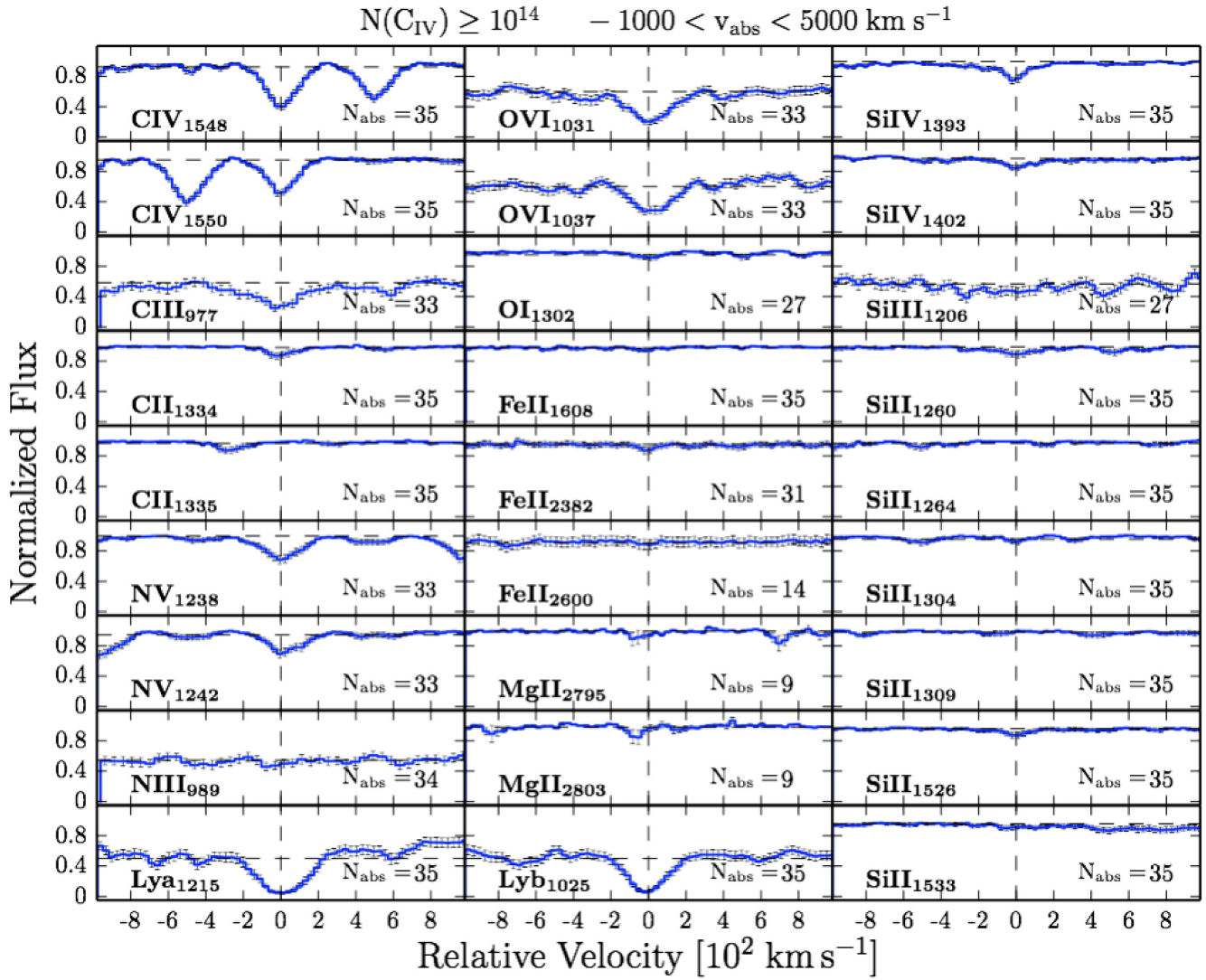


**Figure A4.** Composite spectra for the ions studied in this work, based on C IV systems with  $N(\text{CIV}) \geq 10^{14} \text{ cm}^{-2}$  and  $-1000 < v_{\text{abs}} < 5000 \text{ km s}^{-1}$ . The barycentre position of each C IV system has been computed by weighting the wavelengths with the optical depth of the line profile. Every panel reports the number of absorbers considered to build the stacked spectrum. The error bars are  $1\sigma$  and are estimated by bootstrapping the data using 1000 realizations.

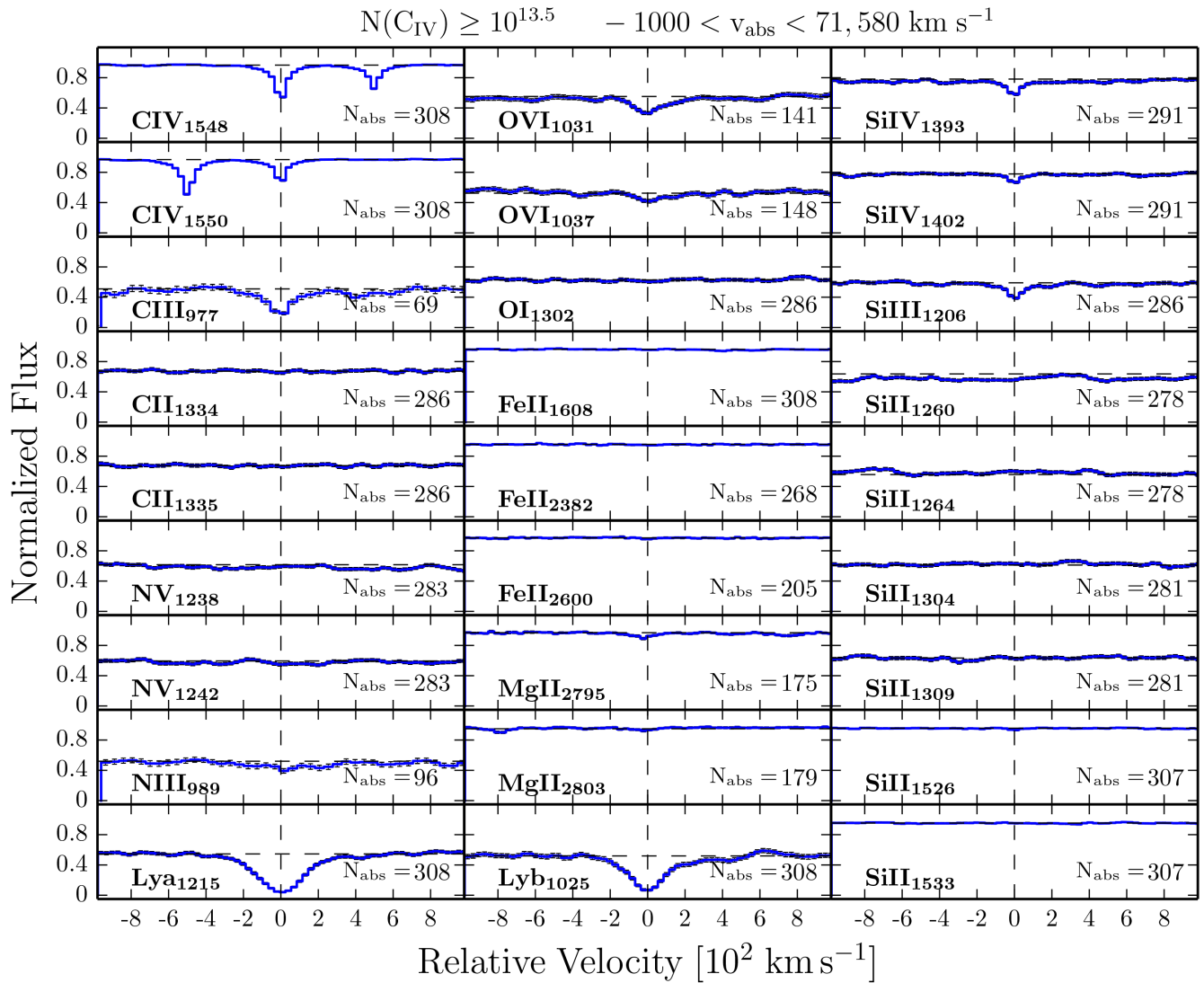


**Figure A5.** Composite spectra for the ions studied in this work, based on C IV systems with  $N(\text{CIV}) \geq 10^{13.5} \text{ cm}^{-2}$  and  $15000 < v_{\text{abs}} < 71580 \text{ km s}^{-1}$ . C IV DLAs are excluded by the stacking. Every panel reports the number of absorbers considered to build the stacked spectrum. The error bars are  $1\sigma$  and are estimated by bootstrapping the data using 1000 realizations. This example demonstrates that the stacking technique applied to the XQ-100 spectra can succeed in detecting absorption lines in the Ly $\alpha$  forest.

This paper has been typeset from a  $\text{\LaTeX}$  file prepared by the author.